Mon. Not. R. Astron. Soc. **000**, 000–000 (0000) Printed 19 January 2000 (MN LATEX style file v1.4)

Cool dust and gas in the Small Magellanic Cloud

S. Stanimirovic,[1,2] ⋆ L. Staveley-Smith,[2] J. M. van der Hulst,[3] Tj. R. Bontekoe,[4,5]
D. J .M. Kester,[6] and P. A. Jones[1]

[1] *University of Western Sydney Nepean, P.O. Box 10, Kingswood, NSW 2747, Australia*
[2] *Australia Telescope National Facility, CSIRO, P.O. Box 76, Epping, NSW 2121, Australia*
[3] *Kapteyn Astronomical Institute, Postbus 800, NL-9700 AV Groningen, the Netherlands*
[4] *Bontekoe Data Consultancy, Herengracht 2 B, 2312 LD Leiden, the Netherlands*
[5] *Astronomical Institute "Anton Pannekoek", University of Amsterdam, Kruislaan 403, 1098 SJ Amsterdam*
[6] *Laboratorium voor Ruimteonderzoek, SRON, P.O. Box 800, 9700 AV Groningen, the Netherlands*

19 January 2000

ABSTRACT

We present high angular resolution far-infrared images of the Small Magellanic Cloud (SMC). The images were reconstructed from data obtained with the Infrared Astronomical Satellite (IRAS), using the Pyramid Maximum Entropy algorithm. The angular resolutions of the images are 1 arcmin at 12, 25 and 60 μm and 1.7 arcmin at 100 μm, which provides an excellent complement to the recent neutral hydrogen (HI) survey from the Australia Telescope Compact Array which has a resolution of 1.6 arcmin. We use the 60 and 100 μm data, together with a standard dust model, to derive a temperature map and a dust column density distribution. Dust temperatures range from 23 to 45 K which is, on average, warmer than for the Galaxy, though there is a deficit of warm, very small dust grains in the SMC. The total amount of cool dust in the SMC is $1.8^{+1.3}_{-0.2} \times 10^4$ M$_\odot$. There is a significant variation of the observed dust-to-gas ratio across the SMC. This may be due to corresponding variations in metallicity, but this explanation is not supported by the limited available data in the literature. Alternatively, there may be a large amount of molecular hydrogen (H_2) in the SMC, $\sim 8 \times 10^8$ M$_\odot$, and/or a large amount ($\sim 10^6$ M$_\odot$) of cold dust (≤ 15 K) not seen by IRAS or COBE/DIRBE. The average dust-to-atomic gas ratio is, by mass, 8.2×10^{-5} which is a factor of ~ 30 below the Galactic value. The spatial power spectrum of the dust column density image can be approximated by $P_{\rm d}(k) \propto k^{-3.1}$ which shows that, as with the HI power spectrum, there is no preferred scale size for dust clouds. A spatial coherence analysis shows that, over a wide range of spatial scales ($\gtrsim 50$ pc), HI and dust are well correlated (> 60 %).

1 INTRODUCTION

The SMC is the third member of an interacting threesome of galaxies (Murai & Fujimoto 1980), the other members of which are the Large Magellanic Cloud (LMC) and the Galaxy. Being of the lowest mass, the SMC is the most disrupted by the apparently gravitational nature of the interactions (Putman et al. 1998), and its large-scale morphology is complex and not fully understood. However, the SMC is extremely rich in neutral atomic gas (Staveley-Smith et al. 1998), and is the site of several giant HII regions and numerous molecular clouds (Rubio, Lequeux & Boulanger 1993). It is of interest as an extremely nearby example of star-formation in an almost primordial medium with low heavy element abundance (Sauvage & Vigroux 1991) and high UV-bright interstellar radiation field (Lequeux et al. 1989). Its proximity makes it possible to obtain data on size scales of a few parsecs and less, but it is also far enough away that all objects are at much the same distance which is relatively well-determined at ~ 60 kpc† (Westerlund 1991).

Being a gas-rich system, the most important component of the cool ISM in the SMC is neutral hydrogen (HI) which we have recently studied using aperture synthesis mosaicing (Staveley-Smith et al. 1997; Stanimirovic et al. 1999). However, there are other important tracers of the cool ISM such as ionized carbon which provides an important cooling line at 158 μm (Kulkarni & Heiles 1989) and dust, which is a source of coupling between neutral and ionized gas, as well as a catalyst for the creation of molecules in dense regions (Dyson & Williams 1997).

A study of dust and gas in the SMC can help us to address various astrophysical questions, such as the following.

† Throughout this paper we assume a distance to the SMC of 60 kpc.

(i) How does the morphology and the phase-mix of the ISM in a low-metallicity, less-evolved galaxy differ from that in a well-evolved galaxy, such as our Galaxy?

(ii) What triggers star formation? Is there a threshold density of gas necessary for the star burst (Knapp 1990)? What is the aftermath of star formation on the ISM?

(iii) Once initiated, by what detailed mechanisms does star-formation propagate in a galaxy where density waves are unimportant?

(iv) How does metallicity evolve with time (Knapp 1990)?

(v) Which physical processes cause the starburst-like dust properties of the SMC? Are they dependent on metallicity and/or star formation, and how (Gordon & Clayton 1998)?

In this paper, we concentrate mainly on the dust properties of the SMC and its relation with the cool gas in the ISM. Early studies of the dust properties and the dust-to-gas ratio, undertaken with ground based instruments (Koornneef 1982; Koornneef 1984; Koornneef & Israel 1985; Bouchet et al. 1985; Israel & Koornneef 1988; Martin, Maurice & Lequeux 1989; Lequeux 1989), were limited to the brightest objects in the SMC and covered a negligible fraction of the area of the SMC (Schwering & Israel 1989). The advent of the infrared all-sky survey by the Infrared Astronomical Satellite (IRAS) resulted in the first complete IR survey of the SMC, which produced a list of point sources (IRAS Point Source Catalog 1988, henceforth IRAS-PSC) and a series of maps produced from Pointed Observations (POs) (Schwering 1988; Schwering & Israel 1989). While having better resolution, at the time, than the old HI images from the Parkes telescope, these maps compare poorly with the 1.6 arcmin resolution from the Australia Telescope Compact Array survey (Stanimirovic et al. 1999). However, the intrinsic resolution of the IRAS telescope optics is 1 arcmin at 60 μm and 1.7 arcmin at 100 μm. By combining several scans at different position angles, it is possible to reconstruct reliable images with a resolution close to the original diffraction limit, and therefore closer to the HI studies. This has been done for many individual fields using the IPAC HiRes program, and has been done for the Galactic Plane (Cao et al. 1999). Methods are discussed by Rice (1993) and Bontekoe, Koper & Kester (1994).

In Section 2 of this paper, we describe selection and processing of the IRAS survey and PO data, the IR morphology of the SMC, comparison with other IRAS and COBE/DIRBE data, and details of the assumed dust model. In Section 3, the dust temperature, dust column density distribution, the total dust mass and its uncertainty are derived and discussed. We derive the dust-to-gas ratio in Section 4, discuss possible reasons for its spatial variation and compare our results with previous studies. Section 5 investigates spatial power spectra of 60 and 100 μm bands and dust and HI column density images. We discuss further the spatial correlation between dust and HI column density, using the spatial coherency spectrum.

2 DATA AND RESULTS

2.1 HIRAS data

2.1.1 Data origin and processing

The HIRAS program (Bontekoe, Koper & Kester 1994) was used to produce the high resolution IR maps of the SMC from the IRAS all–sky survey data in three sets of scans in conjunction with 14 Pointed Observations (POs). Note that HIRAS should not be confused with HiRes, which uses a maximum correlation technique (Aumann, Fowler & Melnyk 1990). The scan pattern of the data used in this paper is shown in Fig. 1. The addition of the PO's nearly doubled the amount of data, but the main reason for their inclusion is the fact that the SMC survey data are taken predominantly in one direction over the map (i.e. from south-east to north-west), while the POs add scans with various other angles. The quality of the individual images have greatly improved by the PO's inclusion. The dust temperature image in particular was of unacceptable quality when made from survey data alone.

In the calibration procedure, data samples from detectors known to be noisy were discarded and glitches in the data (due to cosmic-ray hits) were identified and removed. The zodiacal emission model was then subtracted from all data scans individually. To provide the calibration consistency between different scans, an iterative 'de-striping' algorithm was applied to account for the baseline differences between the scans. For more details on IRAS data calibration and pre-processing see Assendorp et al. (1995), Bontekoe, Koper & Kester (1994), and Kester & Bontekoe (1994). After subtraction of the zodiacal emission model and subsequent 'de-striping', the zero-point of the data is arbitrary. Since there is no clear selection criterion, a (personal) judgment must be made based on the distribution of all data values. One possibility is to take the fiducial zero point such that typically three to five percent of all the data becomes negative. An alternative, used here, is to determine the half-width at half maximum of the distribution of data values, and subtract this half-width from the value of the mode of the distribution (i.e. where the maximum occurs). Both methods yield the best possible IRAS images, which, however, still require some careful post-processing flat-fielding.

Bayesian data analysis (based on Bayesian probability theory), employed in the HIRAS program, requires an uncertainty for every measured quantity (see Sivia 1996 for an excellent tutorial). This property is used extensively to incorporate known instrumental effects as an extra contribution in the uncertainty of the input data. These instrumental effects include: the lossy data compression scheme on board of the satellite, the detector memory effects and glitches due to cosmic ray hits. Correction for truncation effects in the data digitization is also made. Note that a number of the above calibration steps are performed by comparing the data against fiducial data sampled from a low-resolution map. We have found that a single pre-processing pass of the calibration steps is not sufficient. Therefore, after every convergence of our HIRAS program some further refinements in the calibration can be made against a high-resolution map. Typically three to four iterations are needed until no further improvements seem possible.

The HIRAS program uses the Pyramid Maximum En-

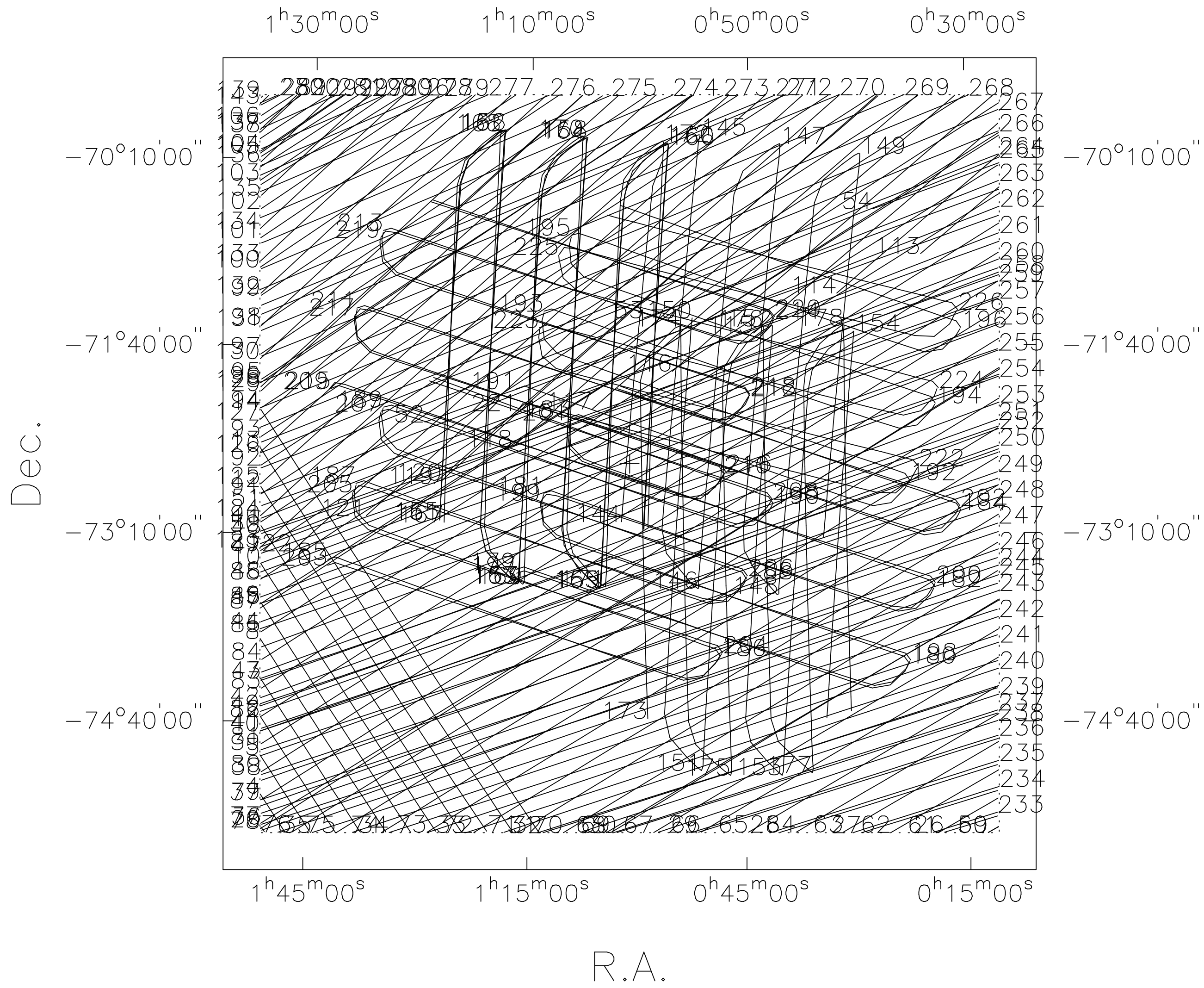

Figure 1. The IRAS scan pattern of the SMC (J2000). Three sets of scans of survey data are present: HCON-1 and HCON-2 (see IRAS Catalogs and Atlases Explanatory Supplement, Beichman et al. 1985), which are almost parallel and run from south-east to north-west, and HCON-3, perpendicular to both but covering just a small area at south-east. 14 DMP Pointed Observations (Young et al. 1985) covering central region of the SMC in various directions are also shown.

tropy (PME) method, an application of the maximum entropy package MemSys5 (Gull & Skilling 1991), to reconstruct reliable images at a resolution approaching the diffraction limit of the IRAS telescope. In the PME algorithm the image is reconstructed in a number of channel images, all computed in parallel, containing respectively 1 by 1 pixels, 2 by 2 pixels, 4 by 4 pixels, 8 by 8 pixels, etc. up to the final pixel number (here 1024 by 1024 pixels). The final image is constructed from the channel images in three steps. First, each channel image is regridded into pixels of the desired map (here 1024 by 1024), and second each regridded image is blurred with a Gaussian profile having a width (standard deviation) of 1.0 times the pixel size in 'its' channel image. Third, the regridded end blurred images are added, pixel by pixel. The final image is thus the sum of several images blurred with Gaussian of different widths. This is a very effective method to reconstruct many spatial scale lengths into a single image, because the entropy acts as a 'filter'. The entropy is the sum of entropies of the channel images, irrespective of the sizes of the pixels. Maximizing this sum ensures that large scale structure is preferentially reconstructed in a channel image with large pixels, because this is 'cheaper in entropy'.

The resulting images of the SMC have a resolution of ~ 1 arcmin for the 12, 25 and 60 μm data and ~ 1.7 arcmin for 100 μm data. As the actual resolution and the dynamic range depend on the local sampling pattern (and source brightness), they vary slightly across the maps. To obtain true intensities from the in-band ones, we have applied colour-corrections from the IRAS Catalogs and Atlases Explanatory Supplement (Beichman et al. 1985). After fitting the observed integrated spectrum with a power law, the correction factors are derived to be 0.93, 0.92, 0.99, 1.00 for

12, 25, 60 and 100 μm, respectively. All images were flat-fielded to remove the residual background.

2.1.2 IR morphology

The resulting high resolution IRAS images of the SMC in all four bands are shown on Fig. 2. The HIRAS data resembles the IR distribution across the SMC found in previous studies, but for the first time contain information on scales as small as ~ 1 arcmin (for 12, 25 and 60 μm) and ~ 1.7 arcmin (for 100 μm). While the 12 and 25 μm images trace mainly hot HII regions and foreground stars with little diffuse IR emission, the 60 and 100 μm data show a lot of diffuse emission with a wealth of filamentary structure. Some residual, low-level stripes (below the 3-σ noise level) are still visible in the 12 and 25 μm images, due to the scan pattern. The astrometric and photometric agreement of point sources with the IRAS-PSC are on average good, although PME fluxes are 10–20 % higher (for more detail on image quality estimate and comparison see Bontekoe, Koper & Kester 1994). As the SMC has a high ecliptic latitude, the contribution of the zodiacal emission is not significant, unlike in the Galaxy where 12, 25 and 60 μm bands are severely contaminated (Schlegel, Finkbeiner & Davis 1998). This, together with the mainly flat and featureless Galactic background around the SMC, enables good reconstruction of the diffuse IR emission.

2.1.3 Comparison with other IR observations

In Table 1 we show a comparison of the integrated flux densities from our data with IR data from three other sources:

(i) COBE/DIRBE maps[‡] for 1.25–240 μm, with a resolution is 0.7 deg. We have applied colour corrections from the COBE/DIRBE Explanatory Supplement (Hauser et al. 1998) and applied a foreground correction, but have not applied any specific zodiacal emission corrections.

(ii) A composite of COBE/DIRBE and IRAS/ISSA maps at 100 μm, corrected for the zodiacal background and colour, with 6 arcmin resolution (from Schlegel, Finkbeiner & Davis 1998). We further applied a correction to remove extended foreground Galactic emission.

(iii) IRAS non-survey 'Pointed Observation' images, corrected for both zodiacal emission and colour, with 8 arcmin resolution (from Schwering 1988).

Flux densities in Table 1 were obtained by summing the maps over an area of 6.25 deg^2 which contains the optical bar and the Eastern Wing (a region seen eastwards of RA $01^{\mathrm{h}}\ 10^{\mathrm{m}}$). Error estimates are dominated by the background corrections and uncertainties in the absolute flux density scale.

Except for the 4.9, 12 and 25 μm COBE/DIRBE data, where the zodiacal emission peaks and the SMC emission is at a minimum, flux densities from all data sources seem to be comparable within 10–20 % uncertainty. We find very good agreement between HIRAS and IRAS fluxes. Surprisingly, integrated flux densities measured by COBE/DIRBE for 60 and 100 μm (from both (i) and (ii)) are higher than HIRAS or IRAS fluxes by about 10–20 %, whereas the IRAS Sky Survey Atlas Explanatory Supplement (Wheelock et al. 1994) gives a linear transformation between IRAS and DIRBE data, in which the IRAS brightnesses are 13% and 28% higher than DIRBE brightnesses at 60 μm and 100 μm, respectively. A possible reason why we measure higher COBE/DIRBE integrated flux densities for the SMC could be a position or resolution dependent brightness transformation between IRAS and DIRBE data.

The integrated HIRAS spectrum of the SMC is shown in Fig. 3 and compared with data from the above three data sources. Flux densities for 0.4 and 0.5 μm were estimated from the blue and visual apparent magnitudes of the SMC, obtained from the Third Reference Catalogue of Bright Galaxies (de Vaucouleurs et al. 1991, henceforth RC 3), and they seem to be consistent (though do not overlap) with COBE/DIRBE data. The stellar radiation is responsible for the $\lambda \lesssim 4$ μm part of the spectrum. The overall spectrum peaks at ~ 100 μm (although in νf_ν units the spectrum peaks at ~ 1 μm). Unlike Galactic IR emission which shows a secondary peak around $\lambda \sim 10$ μm (Cox & Mezger 1989), the SMC IR spectrum has a local minimum at $\lambda \sim 12$ μm. Therefore, the excess near–IR and mid–IR emission is not prominent, indicating that PAH molecules, responsible for IR emission at these wavelengths, play a less important role in the SMC than in the Galaxy.

Quasi-blackbody spectra, $\kappa_\nu B_\nu(T_{\mathrm{d}})$, for dust mass absorption coefficient $\kappa_\nu \propto \nu^{2.0}$ and a range of dust temperatures $T_{\mathrm{d}} = 30, 25, 20, 15$ K, are overlaid on Fig. 3. The far–IR part of the spectrum ($\lambda \gtrsim 45$ μm) seems to be reasonably well–modeled with some combination of the quasi-blackbody curves for temperature range 15–30 K. This means that large dust grains are predominantly responsible for IR emission at $\lambda \gtrsim 45$ μm. The discrepancy for $\lambda < 45$ μm probably corresponds to the presence of some very small grains (VSGs).

2.1.4 SMC dust model & assumptions

The dust model we assume is based on studies by: Mathis, Rumpl & Nordsieck (1977), Draine & Anderson (1985), Dwek et al. (1997), Li & Greenberg (1997), Rodrigues et al. (1997), and consists of:

(i) large silicate and carbonaceous (graphite or amorphous carbon) grains, with sizes $a \gtrsim 0.05$ μm (so–called normal grains)

(ii) very small carbonaceous grains (VSGs), with sizes $a \lesssim 0.005$ μm

(iii) PAH molecules.

While the early dust models in general considered bare silicate and carbonaceous grains, the most recent models are more complex and consider silicate cores coated by the carbonaceous mantle or composite dust grains (collections of very small dust particles loosely attached to one another) (see Li & Greenberg 1997 for a review). The very recent work by Zubko (1999) suggests a dust model for the SMC which consists of a mixture of the silicate core–organic refractory mantle and composite grains, and also includes silicon nanoparticles. However, this model has been fit only to the observational data for the star AzV 398, situated in the SMC bar.

‡ The COBE datasets were developed by the NASA Goddard Space Flight Center under the guidance of the COBE Science Working Group and were provided by the NSSDC.

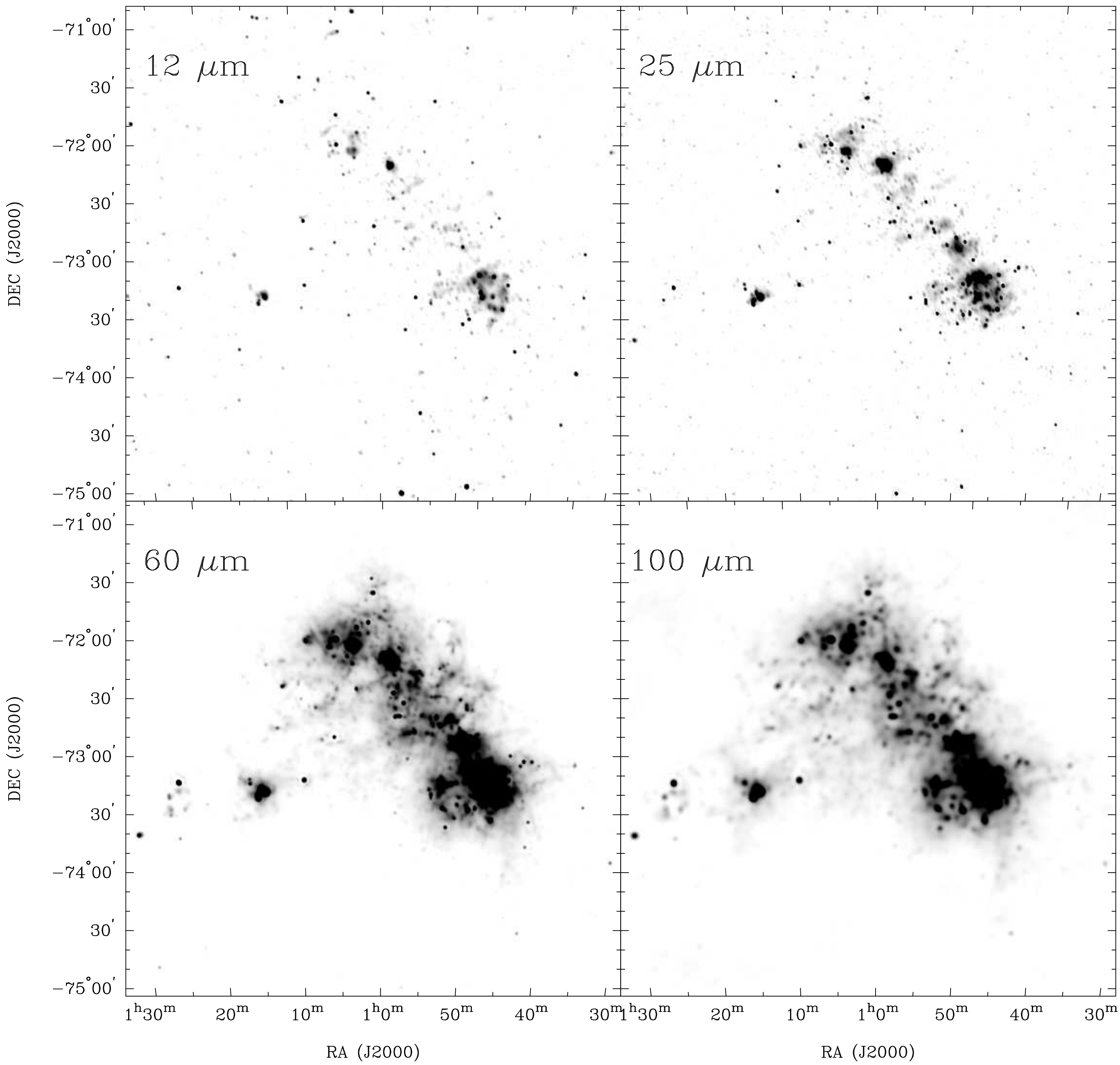

Figure 2. The high resolution PME IRAS images of the SMC at 12, 25, 60 and 100 μm. The grey-scale intensity range is: 0.2 to 1.2, 0.2 to 1.9, 0.6 to 13 and 0.6 to 27 MJy sr^{-1}, respectively, with a linear transfer function. 12, 25 and 60 μm images have resolution of $\sim$ 1 arcmin, while 100 μm image has resolution of $\sim$ 1.7 arcmin.

The main constraint for the abundances of dust grains comes from the SMC extinction curve. Compared to the Galaxy, the SMC has a much straighter, almost linear, extinction curve with: (a) a weaker $\sim$ 0.2 μm bump; and (b) a stronger FUV rise (Lequeux 1989; Sauvage & Vigroux 1991; Gordon & Clayton 1998). Although the carrier of the 0.2 μm bump is still uncertain, it is generally ascribed to the VSGs (Li & Greenberg 1997; Rodrigues et al. 1997). Hence, (a) implies an absence of VSGs particularly responsible for the 0.2 μm bump. However, a significant abundance of VSGs, in general, may still be present in the SMC, as suggested by the integrated IR spectrum for $\lambda < 45$ μm. As the FUV extinction originates from PAH molecules, (b) suggests that the SMC is over-abundant in PAHs, which is in contradiction to the low integrated 12 μm emission (see Table 1), produced mainly by PAHs. Rodrigues et al. (1997) find evidence that the increase of FUV extinction is associated with regions in the SMC protected from the Interstellar Radiation Field (ISRF) (such as molecular clouds). In general, it seems that PAH molecules are not very abundant in the SMC.

The most of the IR emission of the SMC, for $\lambda > 45$ μm, seems to arise from large grains (component (i)). These

Table 1. Comparison of integrated IR flux densities of the SMC from different surveys. The area covered is ~ 6.25 deg^2.

Band (μm)	DIRBE[a] (Jy)	DIRBE + ISSA[b] (Jy)	HIRAS[c] (Jy)	IRAS (POs)[d] (Jy)
1.25	510 ± 25	-		-
2.2	400 ± 37	-		-
3.5	220 ± 31	-		-
4.9	110 ± 43	-		-
12	80 ± 30	-	105 ± 30	147 ± 26
25	460 ± 180	-	310 ± 170	385 ± 56
60	8450 ± 370	-	6700 ± 1060	7170 ± 957
100	15800 ± 2720	15000 ± 2610	13600 ± 1930	13900 ± 1810
140	14000 ± 5600	-		-
240	9600 ± 4400	-		-

[a] COBE/DIRBE data in public domain
[b] from Schlegel, Finkbeiner & Davis (1998)
[c] this paper
[d] from Schwering (1988)

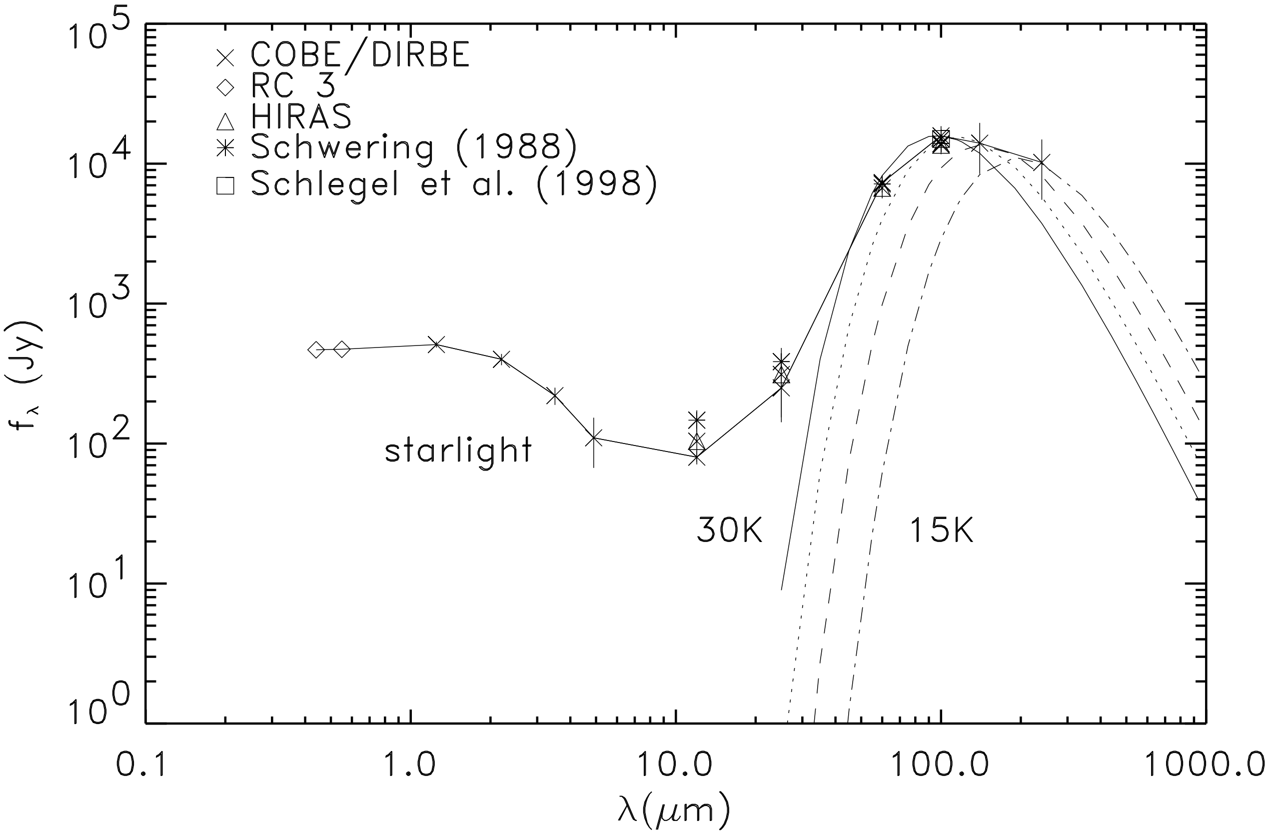

Figure 3. The integrated IR spectrum of the SMC from five different data sources: COBE/DIRBE data (cross), the Third Reference Catalogue of Bright Galaxies (de Vaucouleurs et al. 1991) (diamond), HIRAS data (triangle), Schwering (1988) (asterisk) and Schlegel, Finkbeiner & Davis (1998) (square). The quasi-blackbody spectra for temperature $T_{\rm d}$ = 30 K (solid line), 25 K (dotted line), 20 K (dashed line) and 15 K (dash-dotted line), and assumed dust mass absorption coefficient $\kappa_\nu = 41(\nu/c)^{2.0}$ cm^2 g^{-1}, are overlaid.

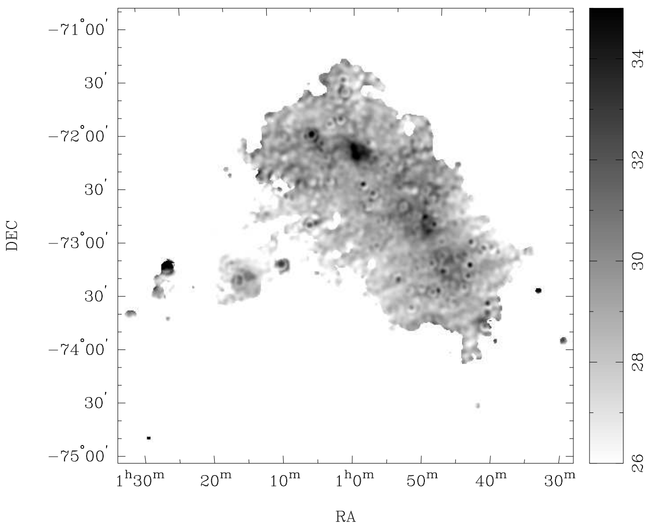

Figure 5. The dust temperature image of the SMC derived from the 60 and 100 μm ratio map. The grey-scale intensity range is 26 to 35 K, with a linear transfer function. The maximum temperature, 45 K, is at position RA $01^{\rm h}24^{\rm m}42^{\rm s}$, Dec $-73°11'45''$ (J2000), which corresponds to N88 (Davies, Elliot, Meaburn 1976).

grains are in thermal equilibrium with the ISRF and radiate as quasi-blackbody emitters within a narrow temperature range (Dwek et al. 1997). We assume that FIR emission is optically thin and that radiation is isotropic. Along each line-of-sight, therefore, IR intensity I_ν is an integral over all dust temperatures:

$$I_\nu = \int_T \rho_T \kappa_\nu B_\nu(T) dT, \tag{1}$$

where ρ_T is the mass density of a dust component at temperature T and κ_ν is the mass absorption coefficient (opacity). The mass absorption coefficient is given by:

$$\kappa_\nu = \kappa_{100\mu{\rm m}}(\lambda/100\mu{\rm m})^{-n}, \tag{2}$$

with n varying between 2.0 for graphite, 1.5 for silicate and 1.0 for amorphous carbon. We assume $\kappa_{100\mu m} = 41$ cm^2 g^{-1} and adopt $n = 2.0$ (Reach et al. 1995; Schlegel, Finkbeiner & Davis 1998) in this paper.

2.2 HI data

The HI data are from a combination of Parkes spectral-line observations with an Australia Telescope Compact Array (ATCA) aperture synthesis mosaic of the SMC (Stanimirovic et al. 1999). The spatial resolution is 98 arcsec, and the velocity resolution is 1.65 km s^{-1}. The area covered is RA $00^{\rm h}30^{\rm m}$ to $01^{\rm h}30^{\rm m}$ and Dec $-71°$ to $-75°$ (J2000), over a velocity range of 90 to 215 km s^{-1}. Fig. 4 shows the integrated column-density image. The total estimated mass of the HI, after correction for self-absorption, is 4.2×10^8 M$_\odot$.

3 DUST TEMPERATURE DISTRIBUTION

The integrated IR spectrum on Fig. 3 and the discussion in Section 2.1.4 indicate that normal grains are the most abundant type of dust grains in the SMC. They emit as quasi-blackbodies at $\lambda \gtrsim 60$ μm within a narrow temperature range. Therefore, under the simplification that along each line-of-sight only one temperature component is present, the ratio of two spectral points of a quasi-blackbody (I_ν) is recursively related to dust temperature $T_{\rm d}$ by:

$$T_{\rm d} = \frac{h(\nu_1 - \nu_2)}{k \ln\left((\frac{\nu_1}{\nu_2})^{3+n} (\frac{I_{\nu_2}}{I_{\nu_1}}) + C_{\rm T} \right)} \tag{3}$$

with h and k being Planck's and Boltzmann's constants respectively, n being exponent of the absorption coefficient ($n = 2.0$) and $C_{\rm T}$ being a temperature-dependent correction factor:

$$C_{\rm T} = \left(1 - (\frac{\nu_1}{\nu_2})^{3+n} (\frac{I_{\nu_2}}{I_{\nu_1}})\right) \exp\left(\frac{-h\nu_2}{kT_{\rm d}}\right) \tag{4}$$

(Schwering 1988). However, Schwering (1988) shows that using $C_{\rm T} = 0$ at the 60 and 100 μm bands introduces an error of only 1 K in dust temperature determinations, if $T_{\rm d} < 45$ K.

To match the point-spread functions of 60 and 100 μm images, both images were smoothed to 2.3 arcmin resolution and the 60-to-100 μm ratio image was derived. Further, applying equation (3), with the assumption that $C_{\rm T} = 0$, and with a 4-σ flux cut-off (to stop noise from propagating), we derive the dust temperature image.

The resultant dust temperature image is shown in Fig. 5. The temperatures vary from 45 K close to HII regions in the optical bar and the Eastern Wing (e.g. N88), dropping to 23 K at the outskirts of the SMC. To compare with the previous results of Schwering (1988), we identify three different temperature regimes in Fig. 5:

(i) $23 < T_{\rm d} < 29$ K – corresponds to diffuse emission originating from dust heated by the ISRF and covering $\sim$ 54 % of the area.

(ii) $29 < T_{\rm d} < 31$ K – corresponds to the hot diffuse emission in the environment of prominent HII regions and covering $\sim$ 39 % of the area.

(iii) $31 < T_{\rm d} < 45$ K – corresponds to discrete hot HII regions and covers $\sim$ 7 % of the area shown in Fig. 5.

Because of our greater resolution, the overall temperature range we find is greater than that measured by Schwering (1988). Surprisingly, though, we find that the diffuse dust component (i) is much more extensive than the negligible figure suggested by Schwering.

Fig. 6 shows the dust temperature, integrated along the optical major axis (position angle 40°), as a function of distance along the minor optical axis. The optical bar of the SMC, the Eastern Wing and HII regions N88 and N81 are very prominent. The decrease of the dust temperature towards the edges of the optical bar and Eastern Wing (noted above) is now prominent. This is unlike the case for the Galaxy (Sodroski et al. 1994) and probably reflects the expected decrease of the ISRF away from regions of high stellar density in the SMC. In the Galaxy, emission at 60 μm appears to have a component due to very small dust grains which are not in thermal equilibrium. In the SMC, this component appears to be less significant.

For the Galaxy, Sodroski et al. (1994) find that 60–75 % of the far-IR luminosity (at 140 and 240 μm) arises from cold

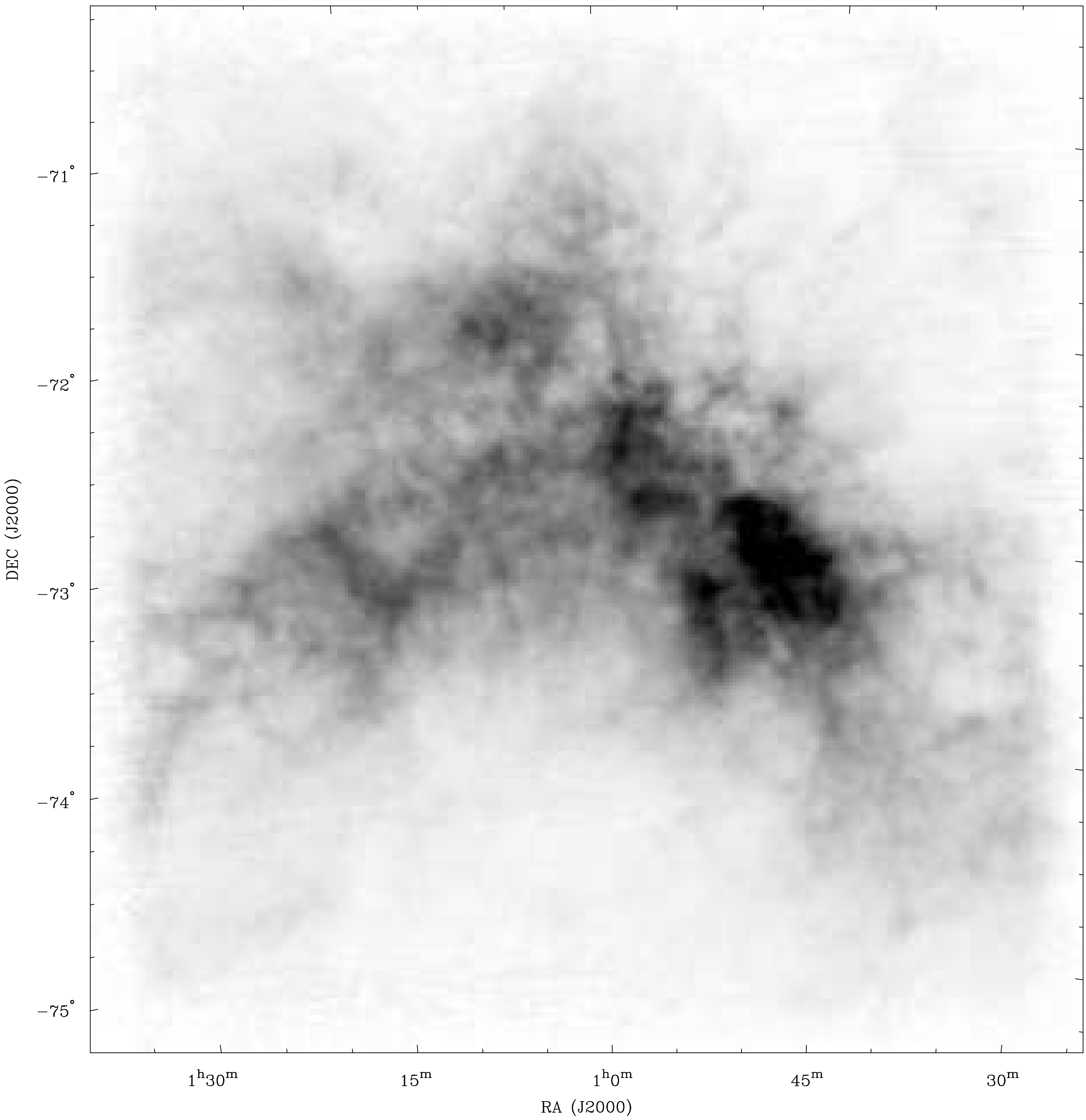

Figure 4. An HI column-density image of the SMC. The grey-scale intensity range is 0 to 1.03×10^{22} atoms cm^{-2} with a linear transfer function. The maximum HI column density, 1.43×10^{22} atoms cm^{-2}, is at position RA $00^{\mathrm{h}}47^{\mathrm{m}}33^{\mathrm{s}}$, Dec $-73°05'26''$ (J2000).

($\sim$ 17–22 K) dust associated with diffuse HI clouds, 15–30 % from cold ($\sim$ 19 K) dust associated with molecular clouds and less than 10 % from warm ($\sim$ 29 K) dust in extended HII regions. These temperature ranges are somewhat lower than we find in the SMC, suggesting that the SMC has a stronger ISRF possibly due to lower metallicity and higher star-formation rate. Schlegel, Finkbeiner & Davis (1998) also find, from 100 and 240 μm full-sky data, that the Galactic dust temperature is lower than that in the SMC, varying between 17 and 21 K.

3.1 Dust mass column density

For a homogeneous object, in the optically thin regime ($\tau_\nu \ll 1$) the dust mass column densities (per unit solid angle) can be calculated from:

$$N_{\mathrm{d}} = \frac{I_\nu}{\kappa_\nu B_\nu(T_{\mathrm{d}})} \frac{1}{\Delta\Omega} \tag{5}$$

where $\Delta\Omega$ is a solid angle corresponding to an area of 1 cm^2 at the distance of the SMC (Schwering 1988). The slow local variation of the dust temperature enables us to use the dust temperature image, with 2.3 arcmin resolution, in

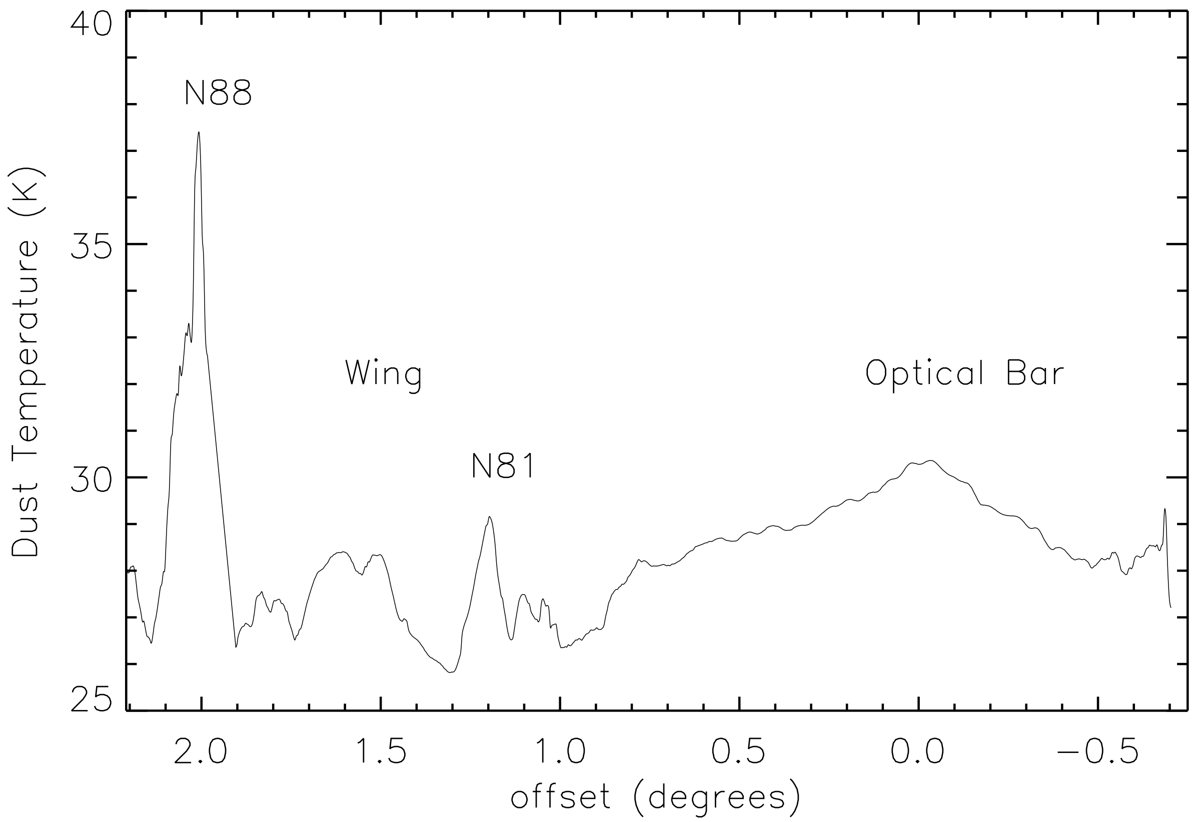

Figure 6. The dust temperature integrated along the optical major axis (at position angle of 40°) and plotted as a function of distance (in degrees) from RA $00^{\rm h}52^{\rm m}$, Dec $-73°00'$ (J2000) along the minor optical axis, starting from south-east.

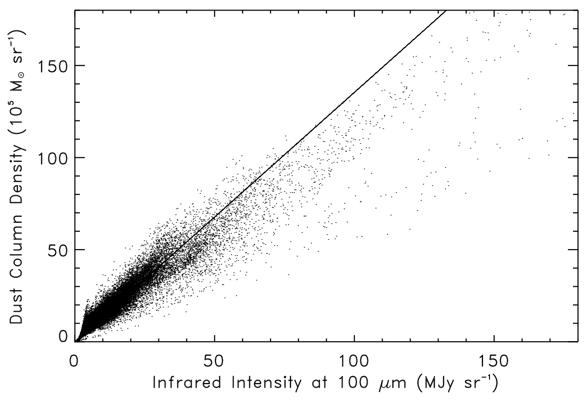

Figure 8. A pixel-to-pixel comparison of the IR intensity at 100 μm (I_{100}) and the dust column density ($M_{\rm d}$), showing a strong correlation. The slope decreases for higher values of I_{100} due to the temperature effect. The linear data fit is overlaid.

conjunction with 100 μm intensity image having 1.7 arcmin resolution. Therefore, the resolution of the derived dust mass column density image is 1.7 arcmin. The distribution of the dust column density across the SMC is shown in Fig. 7. This map shows a wealth of small scale structure, with a variety of filamentary and shell-like features in the optical bar and towards the edges. The column densities range from 0 to 2.1×10^8 M$_\odot$ sr^{-1}, or 0 to 9.4 $\times 10^8$ dust particles cm^{-2} (where a conversion factor from M$_\odot$ sr^{-1} to dust particles cm^{-2} is equal to 4.45 for the mass of an average grain of 1.3×10^{-17} kg taken from Schwering 1988). The highest values correspond to HII regions in the optical bar and Eastern Wing.

Equation 5 shows that the derived value for $N_{\rm d}$ strongly depends on $T_{\rm d}$. For the same value of I_ν, a decrease of $T_{\rm d}$ from 31 K to 23 K would increase $N_{\rm d}$ by a factor of 5. The same equation shows that a strong correlation between I_ν and $N_{\rm d}$ should be expected, as can be seen on Fig. 8. The slope of this correlation decreases for higher values of I_{100} showing that, for higher temperature, IR intensity increases much faster than the dust column density.

3.2 Dust mass ($M_{\rm d}$) and its uncertainty

We estimate an initial value for the dust mass by spatially integrating the dust mass column densities, and obtain $M_{\rm d} = (1.8 \pm 0.2) \times 10^4$ M$_\odot$. Our estimate is slightly higher than derived by Schwering (1988), $M_{\rm d} = (1.4 \pm 0.2) \times 10^4$

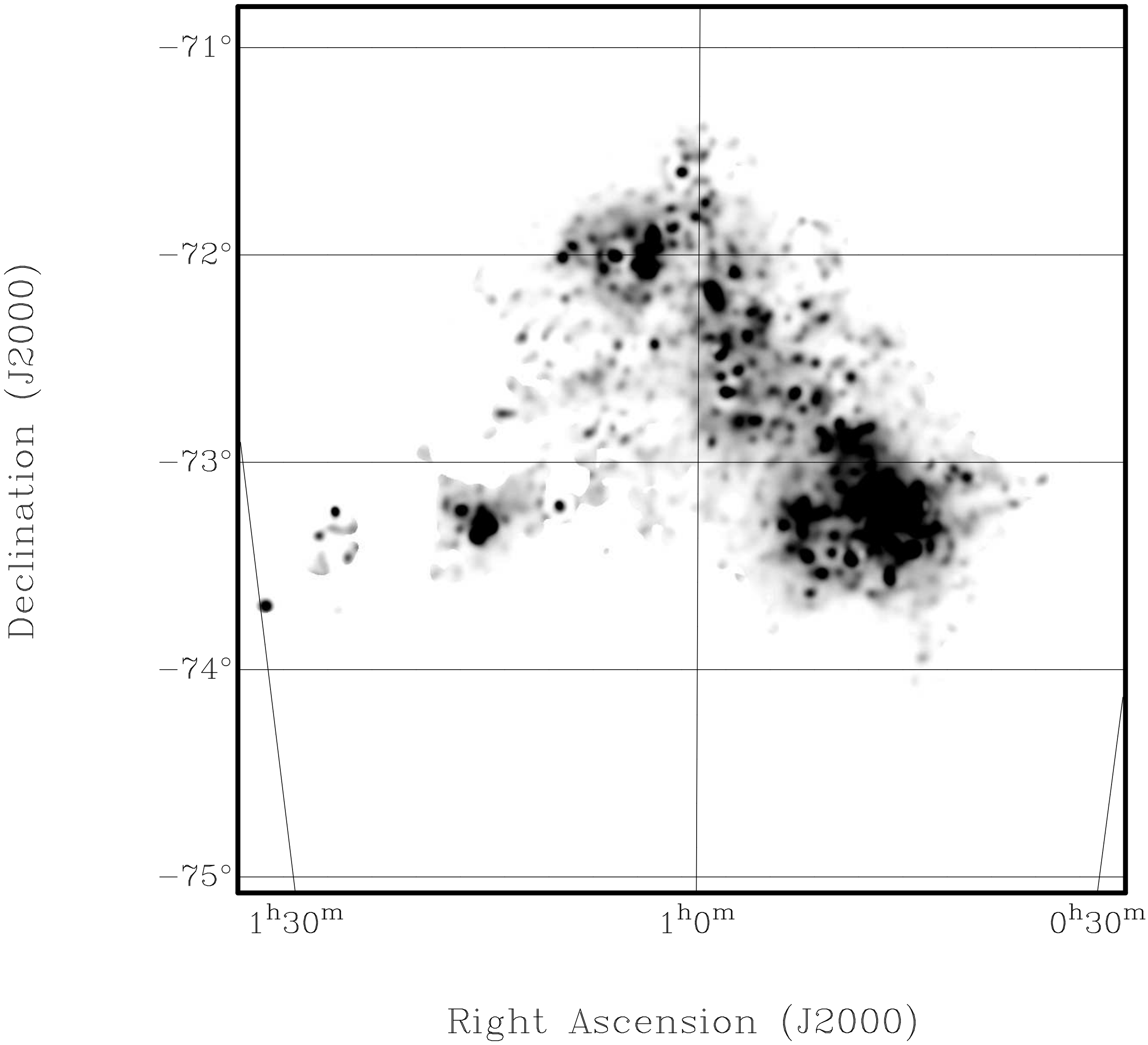

Figure 7. The dust mass column density image of the SMC. The grey-scale range is 0 to 7 $\times 10^7$ $M_\odot$ sr^{-1} with a linear transfer function. The maximum column density is 2.1 $\times 10^8$ $M_\odot$ sr^{-1}. The conversion factor from $M_\odot$ sr^{-1} to dust particles cm^{-1} is equal 4.45. The image has resolution of 1.7 arcmin. A J2000 coordinate grid is overlaid.

$M_\odot$, most of the difference being due to the wider temperature range present in our higher-resolution data. The slightly different area used for the integration of dust column density may also contribute.

Although dust grains emit within a narrow temperature range, a line-of-sight can pass through regions with a different ISRF and therefore with different dust temperature components. Hence, for an object with a large line-of-sight depth, the assumption of a single dust temperature along each line-of-sight might be a crude approximation. This is the main uncertainty in the derived dust mass (M_d) (Draine 1990). To estimate how big the effect can be, we compare the data with a simple dust model from Schlegel, Finkbeiner & Davis (1998).

If a region in the SMC contains an amount (M_{23}) of dust at temperature 23 K, plus a mass fraction f_T of dust at temperature T, IR intensities corresponding to these two temperature components are given by:

$$I_\nu^{23} = \frac{M_{23}}{\alpha_\nu e^{h\nu/23k}} \tag{6}$$

$$I_\nu^{\mathrm{T}} = \frac{M_\mathrm{T}}{\alpha_\nu e^{h\nu/k\mathrm{T}}}, \tag{7}$$

where $\alpha_\nu = c^2/\kappa_\nu 2h\nu^3$. The measured IR intensity is then equal to a sum of both intensity components: $I_\mathrm{tot}(\nu) = I_\nu^{23K} + I_\nu^{\mathrm{T}}$.

Under the assumption of a single dust temperature along a line-of-sight, $I_\mathrm{tot}(\nu)$ for both 60 and 100 μm is used in equation 3 to estimate the dust temperature T', which will have a value between 23 K and T. This provides a further estimate of the dust column density and dust mass M'_d in the region, which is always less than the true dust mass.

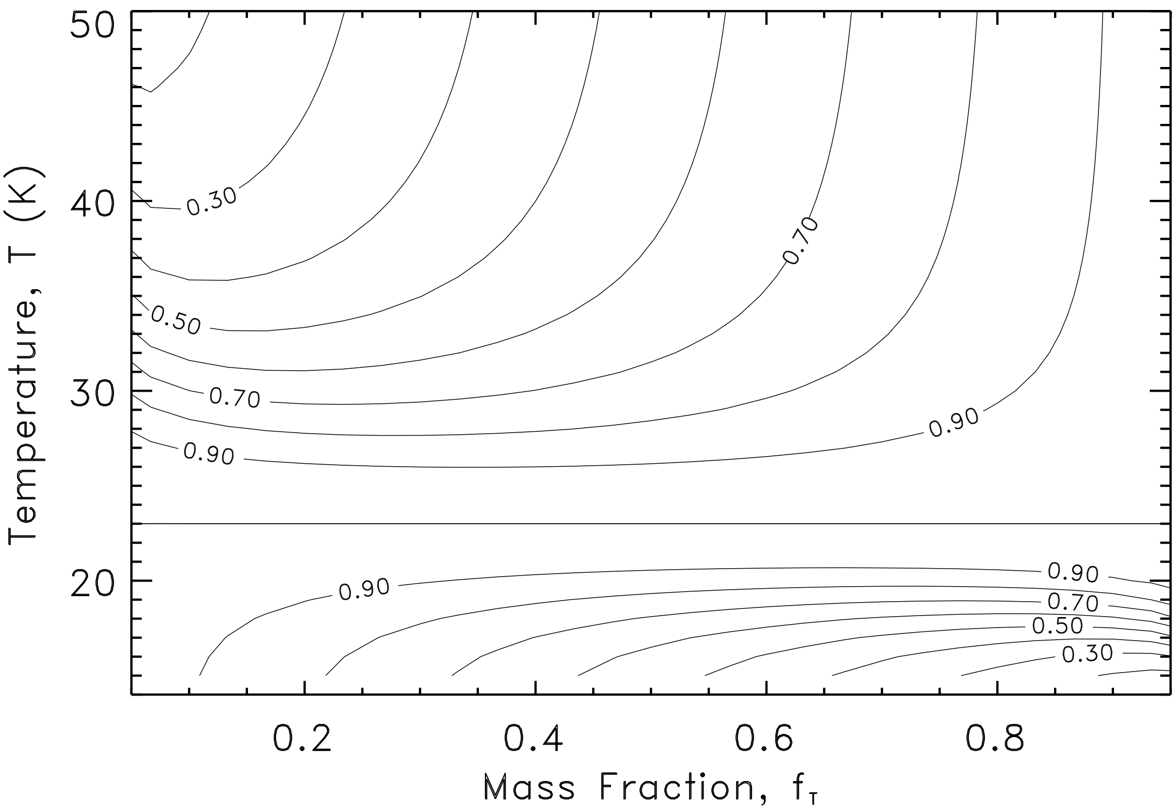

Figure 9. Contours of the ratio of the recovered and true dust mass plotted as a function of temperature and the mass fraction $f_{\rm T}$ of dust at temperature T. Following Schlegel, Finkbeiner & Davis (1998), this plot illustrates how much the true dust mass can be underestimated if a single temperature is assumed where two temperatures are present (23 K and T).

However, if we consider both temperature components present, the dust mass is simply:

$$M_{\rm d} = M_{23} + \frac{f_{\rm T}}{(1 - f_{\rm T})} M_{23}. \tag{8}$$

The ratio of recovered ($M'_{\rm d}$) and true dust mass ($M_{\rm d}$) is then given by:

$$R(f,T) = \frac{M'_{\rm d}(f_{\rm T}, T)}{M_{\rm d}(f_{\rm T})} \tag{9}$$

and is a two-dimensional function of $f_{\rm T}$ and T, bounded by 1. For a range of mass fractions of the second component, $f_{\rm T}$, and a range of temperatures of the second component, T, Fig. 9 shows contours of the ratio of recovered dust mass and true dust mass.

Assuming a single dust temperature model, we have calculated (Section 3) temperatures in the SMC to be in the range 23–45 K, with the temperature of the diffuse dust component in the range 23–31 K. From Fig. 9, for $19 < T < 30$ K, the true dust mass is underestimated by < 30 %. Temperatures higher than 31 K (e.g. near HII regions) only occur in a small area of the SMC (~ 7 %) and probably do not contribute significantly to an underestimate of the dust mass.

Another important source of uncertainty in the derived dust mass is cold dust. Because of the quasi-blackbody cooling nature of dust grains, $I_\nu \propto T^{4+n}$, cold dust (< 20 K) does not contribute significantly to the IR intensity. Therefore, a large amount of cold dust can be masked by the presence of a small amount of cool (~ 25 K) or warm (~ 50 K) dust.

The lower limit for dust temperature, contributing to IR emission at 100 μm, in the Galaxy is 17 K (Schlegel, Finkbeiner & Davis 1998). For a sample of nearby spiral galaxies, Alton et al. (1998) found that a cold dust component at 18–21 K and heated by the general ISRF, is prominent at larger radii. Since the SMC has a stronger ISRF than the Galaxy, we would not expect dust in the SMC to be cooler than dust in the Galaxy. Taking 17 K, therefore, as a lower limit for the temperature of cold dust in the SMC, we find from Fig. 9 that the total dust mass would be at most underestimated by 60 %. A similar estimate was found in Schwering (1988) using different methods. This provides an estimate of the total dust mass in the SMC, $M_{\rm d} = 1.8^{+1.3}_{-0.2} \times 10^4$ M$_\odot$.

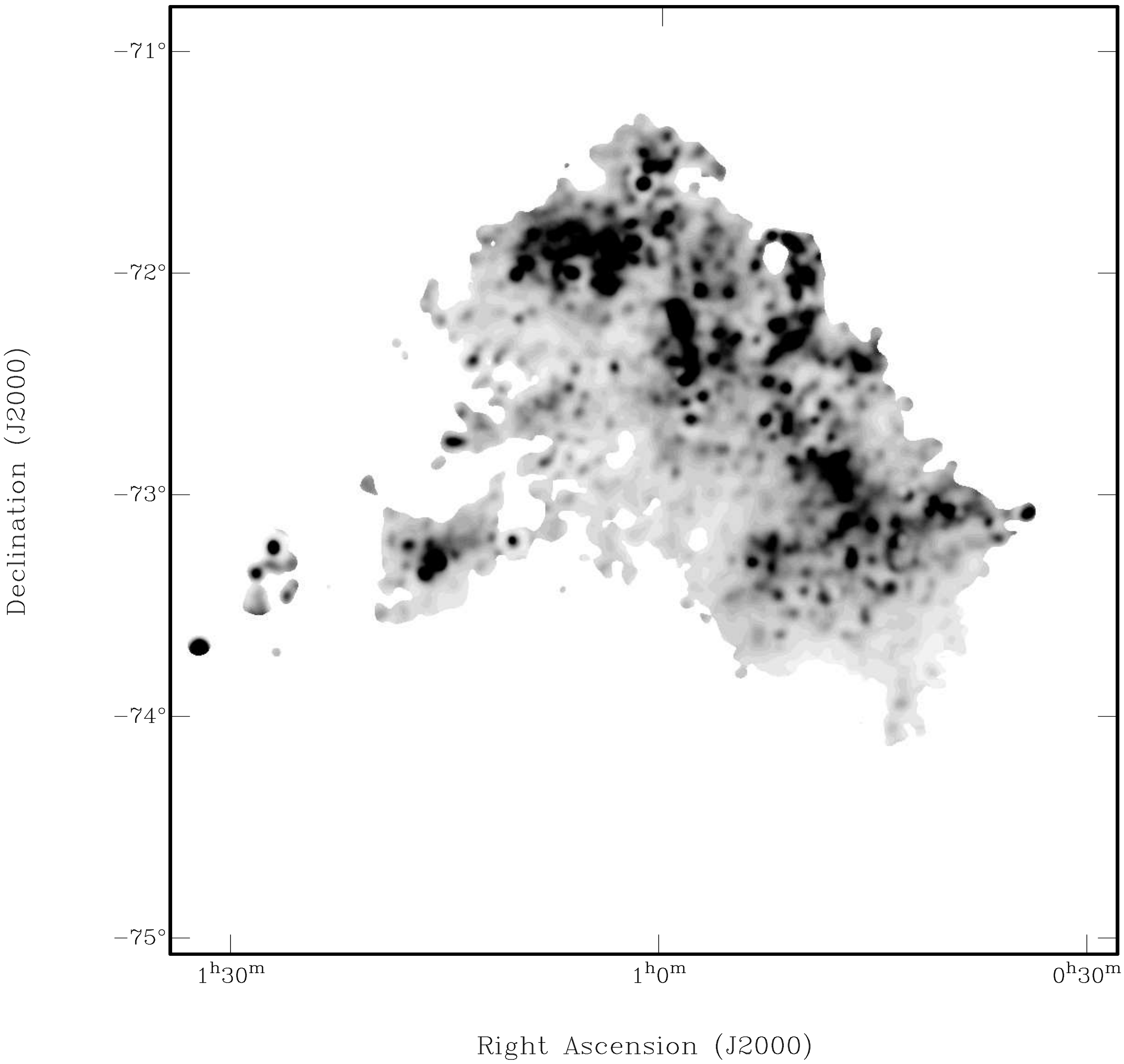

Figure 10. The dust-to-gas mass ratio image of the SMC. The grey-scale range is 0 to 10^{-4}, with a linear transfer function. The maximum dust-to-gas mass ratio of 6×10^{-4} corresponds to N88 and is at position RA $01^{\rm h}24^{\rm m}3^{\rm s}$, Dec $-73°13'45''$ (J2000).

4 DUST-TO-GAS MASS RATIO

The comparison of the IR intensity, at all wavelengths from 100 μm to 1 mm, and HI column density in the case of our own Galaxy have shown a good linear correlation for low flux levels (Schlegel, Finkbeiner & Davis 1998; Boulanger et al. 1996), with $I_{100} \approx 0.5 W_{\rm HI} + 0.3$ ($W_{\rm HI}$ is velocity-integrated HI brightness temperature in units of K km s^{-1}). Substantial scatter has been found for higher flux levels and has been usually attributed to the presence of molecular hydrogen. In the case of the SMC, Schwering (1988) has noted a good qualitative correlation between the IRAS 100 μm intensity and HI column density (using radio data from McGee & Newton 1981), with remarkable differences in some cases (such as N66), where he suggests gas is either completely blown away or in molecular form. It was also found that $I_{100} \propto N_{\rm HI}^{\beta}$, with $\beta = 2.2$, showing that IR intensity increases with the HI column density much faster in the SMC than in the Galaxy. The HIRAS data at 100 μm and the HI column density, used here, show similar results: a tight correlation between I_{100} and $N_{\rm HI}$ is seen within the optical bar and the central part of the Eastern Wing, while in the Eastern Wing in general and especially in the region between the optical bar and the Wing, the correlation is much weaker.

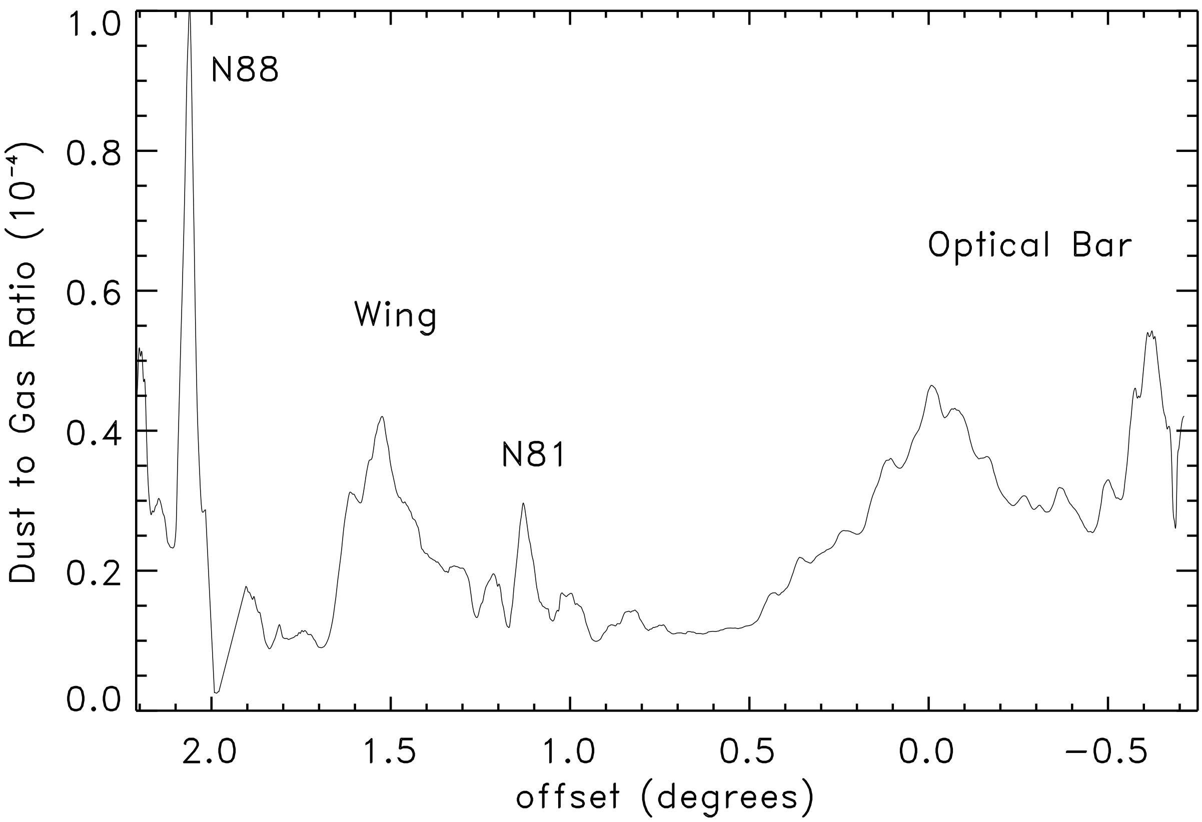

Figure 11. The dust-to-gas mass ratio integrated along the optical major axis (at position angle of 40°) and plotted as a function of distance (in degrees) from RA $00^{h}52^{m}$, Dec $-73°00'$ (J2000) along the minor optical axis, starting from south-east. This slice has the same resolution as the one on Fig. 6.

To compare HI column density with the dust mass column density, we first apply corrections for self-absorption to the HI data (Stanimirovic et al. 1999) and obtain the total HI column density. The dimensionless dust-to-gas mass ratio, derived by dividing dust and HI (mass) column density images (D_g), is shown in Fig. 10. The image has a range between 0 and 6×10^{-4}, showing that the gas content (by mass) in the SMC is much higher than the dust content. A significant variation of D_g is visible across the SMC, with a variety of small scale features. The main impression the dust-to-gas ratio image leaves is a 'granulated' appearance revealing various HII regions with a significantly higher dust-to-gas mass ratio relative to the spatially averaged value across the whole SMC of 2.5×10^{-5}. It is believed that the gas and dust are well mixed together in the ISM (Cox & Mezger 1989). The local variation of the dust-to-gas ratio therefore may reflect more local phenomena, such as:

(i) an atomic gas deficiency due to H_2 formation;
(ii) excess dust created in regions of massive star formation; and
(iii) the presence of cold dust not emitting at 100 μm.

Similar variation of D_g in the SMC has been noted in Schwering (1988) (with a peak of 1.5 $\times10^{-4}$), who has attributed most of it to the presence of a significant amount of molecular gas (i.e. (i)). We address this question in Section 4.2. In Fig. 11 we show the dust-to-gas mass ratio integrated along the optical major axis and plotted as a function of distance from the optical bar. This profile, together with Fig. 10, distinguishes a few regions with a significantly different values of D_g.

4.1 D_g in discrete HII regions

The highest values of the dust-to-gas ratio are found in discrete bright HII regions (e.g. N81 and N88). HII regions as, in general, sites of the most recent star formation are usually located on the edges or embedded in the clouds of dense and cold gas (Gordon 1988). The brightest HII regions in the SMC are usually found to be larger and more diffuse than the ones in the Galaxy (Copetti 1990), and their morphology can be explained by the metallicity effect. Being in such a low-metallicity environment, the size of the CO-emitting core within a molecular cloud, associated with an HII region, shrinks while the photon-dominated region (PDR) simultaneously increases its volume (Israel et al. 1996).

The 100 μm IR emission and also HI emission, associated with an HII region, come from a dense layer surrounding the HII region (Gordon 1988). These layers are usually dust and gas rich with dust temperatures (in the SMC) of 31–45 K. Kurt et al. (1995) and Kurt & Dufour (1998) examined abundances of C, N and O in a few HII regions in the SMC. They find that, for N88 in particular, the O/H ratio is not indicative of O enrichment arising from mass loss. This is supportive of case (i) (Section 4) for the excess dust associated with N88. The O/H ratio found for N88 is very similar to values found in a few other HII regions in the SMC. A similar effect has been found in the Galaxy where Reach, Wall & Odegard (1998) find that most of their excess IR emission from high latitude clouds comes from dust associated with molecular gas.

4.2 Hidden gas, hidden dust or a real dust-to-gas gradient?

Both the optical bar and the Eastern Wing show in general a similar large-scale trend in $D_{\rm g}$, peaking in the middle of the region, where most of the recent star formation is concentrated, and having a steep decrease towards the edges (Fig. 11). Diffuse regions in the immediate environment of HII regions have a dust-to-gas ratio very close to the estimated spatial average value (2.5×10^{-5}). Being less exposed to the strong radiation field, their gas content is mostly atomic. Since the IR intensity at 30 K peaks around 100 μm, the measured dust mass is reasonably well-estimated. Therefore, the estimated values for the dust-to-gas ratio for these regions are probably accurate.

An interesting feature stands out on Fig. 11. The dust-to-gas ratio drops significantly in the region between the bar and the Eastern Wing. The measured dust temperature here reaches almost the minimum value (23 K). If a significant amount of dust cooler than 23 K is present, an underestimate of the total dust mass could explain the decrease in $D_{\rm g}$ (case (iii) in Section 4). In the study of a sample of nearby, spiral galaxies, Alton et al. (1998) indeed found that cold dust ($T_{\rm d} \leq$ 18–21 K) is more prevalent at larger galactic radii.

On the other side, further towards the west from the middle of the bar, the profile on Fig. 11 shows, interestingly, a secondary maximum almost at the edge of the bar. This increase mainly comes from the loop-like feature shown in Fig. 10. This feature is associated with the HI shells: SMC HI-199, SMC HI-202 and SMC HI-170 (see Staveley-Smith et al. 1997) and with the several neighboring HII regions. Most likely, molecular gas formation (case (i), Section 4) is again responsible for the high value of $D_{\rm g}$.

Let us try now to explain the observed variation of $D_{\rm g}$ as a result of local phenomena (i) and (iii) only. We assume first that the real value of the dust-to-gas ratio is around 1.25×10^{-5} in the region between the optical bar and the Eastern Wing, and that all values for $D_{\rm g} > 1.25 \times 10^{-5}$ come from the atomic gas deficiency due to the presence of significant amount of molecular hydrogen. Measuring the dust and HI mass in the regions of the SMC where $D_{\rm g} > 1.25 \times 10^{-5}$, we can estimate the mass of the molecular hydrogen which needs to be added so that the dust-to-total gas ratio in the SMC can everywhere have a constant value of 1.25×10^{-5}. The result is that the required mass of molecular hydrogen is about 8.4×10^{8} M$_{\odot}$, i.e. ~ 2 times that of atomic hydrogen, and almost 30 above the estimated mass of H_2 of 3×10^{7} M$_{\odot}$ from CO observations (Rubio, Lequeux & Boulanger 1993). The total H_2 mass of the SMC of $(0.75 \pm 0.25) \times 10^{8}$ M$_{\odot}$, estimated by Israel (1997), after a re-examination of the CO to H_2 conversion factor, is still more than 10 times lower than here suggested value. We therefore conclude that the assumption, in which all dust excess comes from the molecular gas, appears to be untenable.

Table 2. An estimate of the mass of cold dust having temperature of 15, 12, 10 or 8 K. Values are derived under assumption that a particular dust temperature (at 15, 12, 10 or 8 K) is entirely responsible for the total luminosity at 240 μm, obtained from the low-resolution COBE/DIRBE data.

Temperature (K)	Mass (M$_{\odot}$)
15	2.4×10^{4}
12	9.5×10^{4}
10	3.7×10^{5}
8	2.9×10^{6}

Another alternative for the variation in $D_{\rm g}$ (of almost a factor of 3) is the presence of cold dust, not seen at 60 or 100 μm. The low-resolution COBE/DIRBE data at 140 and 240 μm give the best available constraint on dust content on temperatures < 20 K. The 240/140 μm ratio map is noisy and has low resolution (0.7 deg) but provides evidence for temperatures as low as 15 K, somewhat lower than the HIRAS lower limit of 23 K. If we assume that all of the 240 μm luminosity, Fig. 3, arises from dust at 15 K, then the 'hidden' cold dust mass is $\sim 2.4\times10^{4}$ M$_{\odot}$. This is still insufficient to explain the variation in $D_{\rm g}$. However, at lower temperatures there can be even larger amount of dust present, as shown on Table 2. It is questionable whether such a large amount of cold dust can exist in the SMC. Future observations at sub-millimeter wavelengths are necessary in order to determine if such dust is present and, if so, what its origin is and what role it plays in the ISM.

However, for the time being, it appears that neither the atomic gas deficiency due to hidden H_2, nor the presence of hidden cold dust can explain the derived variation of $D_{\rm g}$. Although a combination of these effects most likely plays an important role, the existence of the third scenario, the intrinsic spatial variation of $D_{\rm g}$, seems to be very likely. Intrinsic radial gradients in $D_{\rm g}$ have been seen in several nearby spiral galaxies (Viallefond, Goss & Allen 1982; Viallefond & Goss 1986; Walterbos & Schwering 1987; van der Hulst et al. 1988; Issa, McLaren & Wolfendale 1990) and in our own Galaxy (Sodroski et al. 1997). Sodroski et al. (1997) explain a decreases of $D_{\rm g}$ with increasing Galactocentric distance as being due to a decrease of the stellar efficiency in recycling of the disk material. As dwarf galaxies, in general, have stochastic star formation and chemical evolution, it is usually hard to notice any radial dependence in their $D_{\rm g}$ (Issa, McLaren & Wolfendale 1990). The significant large-scale trend in $D_{\rm g}$ in the SMC, from the optical bar to the Eastern Wing (Fig. 11), may suggest a radial gradient of $D_{\rm g}$, seen for the first time in a dwarf galaxy.

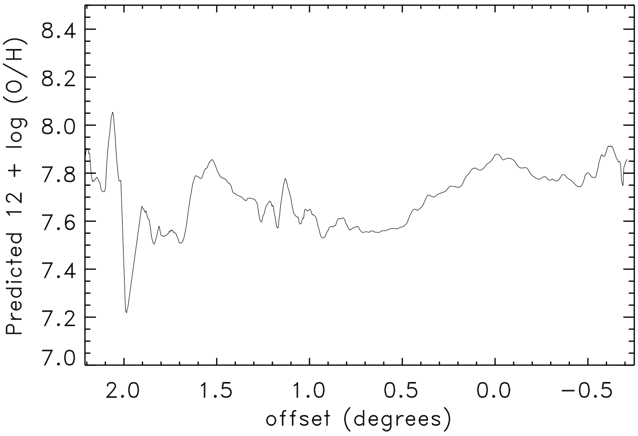

Figure 12. The predicted variation of the oxygen abundance in the SMC for the profile of the dust-to-gas mass ratio shown on Fig. 11 using the correlation found by Lisenfeld & Ferrara (1998). The profile was scaled using the metallicity of HII region N88 from Kurt et al. (1995).

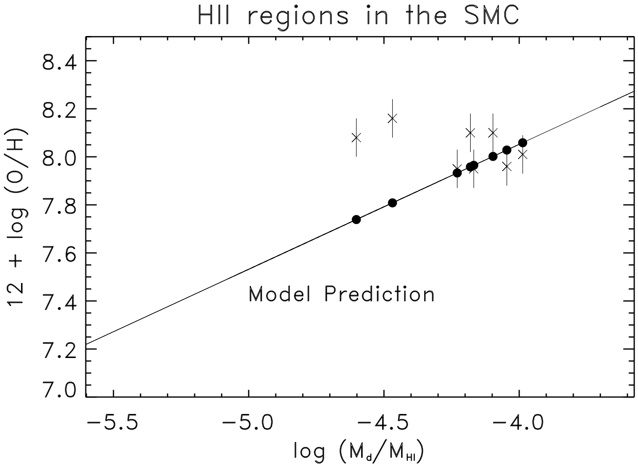

Figure 13. The correlation between the dust-to-gas mass ratio and the oxygen metallicity suggested by Lisenfeld & Ferrara (1998), scaled by the metallicity of HII region N88 from Kurt et al. (1995) and plotted with the solid line. Several HII regions in the SMC, from Dufour & Harlow (1977), Pagel, Edmunds & Fosbury (1978) and Kurt & Dufour (1998), are shown with crosses. Their oxygen metallicities predicted by the correlation are shown with filled circles.

4.3 The relationship between $D_{\rm g}$ and metallicity

Dwek (1998) has presented a model for the dynamical and chemical evolution of dust abundances and composition in the ISM of the Galaxy. In this model, the grain life-cycle starts with the grain formation in quiescent stellar outflows and/or explosive eruptions of novae and type II supernovae. Once formed, dust grains get ejected into the ISM where they are further processed under exposure to various processes which influence their abundance and physical properties. While various processes in the ISM are very destructive for dust grains, the grain growth by the accretion process plays a very important role in establishing the dust mass.

The Dwek (1998) model predicts that $D_{\rm g}$ decreases with the galactocentric radius and that its decrease tightly follows the ISM metallicity, regardless of the star formation history of the ISM. The correlation between $D_{\rm g}$ and metallicity appears to be a consequence of the fact that the relative efficiency of the grain destruction and grain accretion processes is constant with time. Both the $D_{\rm g}$ radial dependence and the correlation with metallicity agree well with the observational results for the Galaxy by Sodroski et al. (1997). The variation of $D_{\rm g}$ in the SMC may also probe metallicity variations and the evolutionary history of the SMC.

Further support to the dust evolutionary model by Dwek (1998) is given by Lisenfeld & Ferrara (1998) who examined the variation of $D_{\rm g}$ with metallicity in a sample of dwarf galaxies (including the SMC). They found a correlation between oxygen abundance and dust-to-gas mass ratio given by:

$$12 + \log {\rm O/H} \propto (0.52 \pm 0.25) \log(M_{\rm d}/M_{\rm HI}). \quad (10)$$

Their trend of metallicity as a function of $D_{\rm g}$ is similar to the trend found by Dwek (1998) in a few different Galactic regions, though with a significant offset. This may be due to the stochastic nature of star formation and chemical evolution in dwarf galaxies and their underestimated dust content (Dwek 1998).

We have applied the correlation from Lisenfeld & Ferrara (1998) to the distribution of $D_{\rm g}$ along the minor optical axis in the SMC, to predict the spatial variation of the oxygen abundances. The profile is plotted on Fig. 12 showing a variation by a factor of two along the minor optical axis, which is quite reasonable. Hence, if the suggested relation between the metallicity and $D_{\rm g}$ holds in the SMC, a variation in metallicity across the SMC by factor of ~ 2 could completely explain the observed variation in $D_{\rm g}$.

To test whether the suggested correlation by Lisenfeld & Ferrara (1998) holds in the case of the SMC, we measured $D_{\rm g}$ for a few HII regions with known metallicity (from Dufour & Harlow 1977; Pagel, Edmunds & Fosbury 1978; and Kurt & Dufour 1998). The metallicities predicted by the correlation (filled circles) and the values obtained from observations (crosses) are plotted on Fig. 13. The model is disappointing in that the current HII metallicity data do not fit the predicted correlation, and may even suggest a negative gradient of the oxygen metallicity as a function of $D_{\rm g}$ whose physical meaning would be hard to explain. It should be noted, though, that most of these HII regions are situated in the optical bar and have very homogeneous properties. Therefore, they may not well represent regions with significantly different value of $D_{\rm g}$. Future metallicity measurements of a wider range of objects spread over the SMC are necessary to test the suggested correlation between dust-to-gas ratio and metallicity.

Another important conclusion from the model by Dwek (1998) is that the dust composition (relative abundance of carbon-to-silicate grains) varies with time. As a consequence, several classes of galaxies, with different dust compositions, should be observed. The first class represents young, low-evolved galaxies, where carbon grains are much less abundant than silicate grains. These galaxies have a weak extinction bump at ~ 0.2 μm. According to its extinction curve and the dust grain abundances (see Section 2.1.3

and Section 2.1.4), the SMC may be a typical representative of this category. The second class of galaxies has the extinction curve represented with the Galactic extinction curve, while the model also predicts the existence of the intermediate-age systems, with an excess extinction peak around 0.2 μm, relative to the Galactic one.

4.4 Comparison with previous work

Two methods for determination of the average dust-to-gas ratio are available in the literature:

(1) where the dust mass is determined from measured IR intensities, and the HI mass is determined from 21 cm spectral line observations ($M_{\rm HI}/M_{\rm d}$), as used in this paper;

(2) where the extinction is determined from photometric observations of stars in the SMC ($E_{\rm B-V}$), and the HI mass ($M^{*}_{\rm HI}$) is measured in front of these stars from the profile of the Lyman α interstellar absorption line ($M^{*}_{\rm HI}/E_{\rm B-V}$).

The relationship between these quantities $M_{\rm HI}/M_{\rm d}$ and $M^{*}_{\rm HI}/E_{\rm B-V}$, obtained in these two methods, is given by:

$$\frac{M_{\rm HI}}{M_{\rm d}} = R\left[\frac{M^{*}_{\rm HI}}{E_{\rm B-V}}\frac{m_{\rm d}}{m_{\rm HI}}(1.086\pi a^{2}Q^{\rm ext}_{\rm V})\right]^{-1}, \tag{11}$$

where $R = A_{\rm V}/E_{\rm B-V}$ is the ratio between the visual extinction and the colour excess, a is an average size (radius) of dust grains, $Q^{\rm ext}_{\rm V}$ is the visual extinction efficiency factor, and $m_{\rm d}$ and $m_{\rm HI}$ are masses of an average dust grain and an HI atom, respectively. The conversion strongly depends on parameters R, a and $Q^{\rm ext}_{\rm V}$, whose values are poorly known and also vary from galaxy to galaxy. To compare our results for $M_{\rm HI}/M_{\rm d}$ with values previously found for $M^{*}_{\rm HI}/E_{\rm B-V}$, we have assumed values: $R = 2.72 \pm 0.18$ (Bouchet et al. 1985), $a = 1 \times 10^{-7}$ m (Schwering 1988) and $m_{\rm d} = 1.3 \times 10^{-17}$ kg (Schwering 1988). The estimate of $Q^{\rm ext}_{\rm V}$ is complex and its value depends on grain nature (size and the refractive index of grain material), geometry and a wavelength. We have assumed here value $Q^{\rm ext}_{\rm V} = 1$, estimated for $\lambda = 0.5$ μm and spherical silicate dust grains having radius of 1×10^{-7} m (from Fig. 3.9 in Evans 1994).

In Table 3 we give a comparison of our derived average dust-to-gas ratio with previous estimates. Note that this value was derived from ratio of the total dust mass (1.8×10^{4} $M_{\odot}$) and the total HI mass (2.2×10^{8} $M_{\odot}$), in a $\sim 2^{\circ}\times 2^{\circ}$area of the SMC and shown on Fig 10. All estimates of the average dust-to-gas ratio ($M_{\rm d}/M_{\rm HI}$) in the SMC are quite close, although the conversion parameters between independent methods (1) and (2) (R, a and $Q^{\rm ext}_{\rm V}$) are quite uncertain. The value derived from method (1) in Schwering (1988) is slightly lower than the other ones. The average dust-to-gas ratio derived in this paper is very similar to values obtained by Lequeux (1989) and Martin, Maurice & Lequeux (1989), although two very different methods were used. The estimated average dust-to-gas ratio in the SMC is almost 30 times lower than in the Galaxy, using an average Galactic dust-to-gas ratio of 1/375 from Schwering (1988).

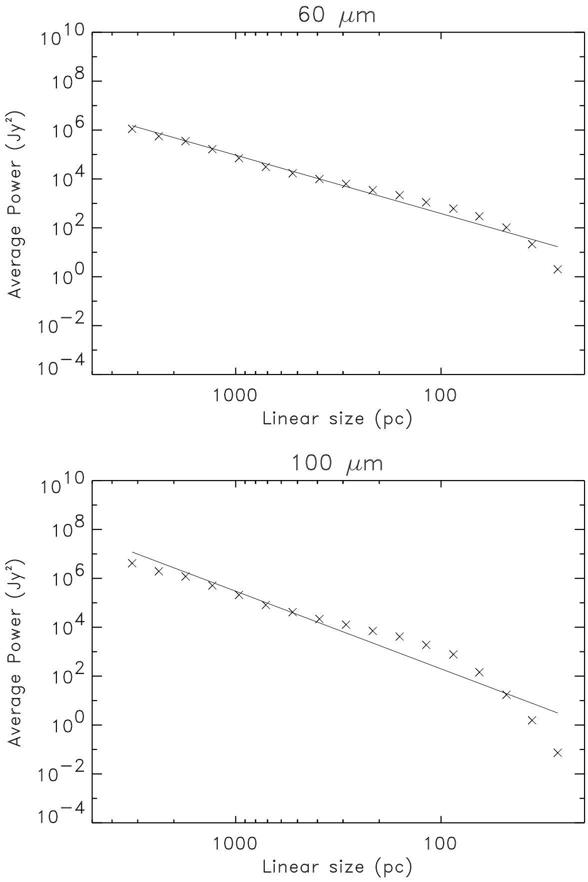

Figure 14. The 2-D spatial power spectrum of the 60 and 100 μm intensity images. Linear size L, is related to the radius k in the uv-plane by $L(\text{pc}) = d/k(\lambda)$, where $d = 60 \times 10^{3}$ pc is the distance to the SMC (1 kpc corresponds to 57.3 arcmin and 60λ). Least-square fits, derived using all data points, are overlaid.

5 STATISTICAL INVESTIGATION OF DUST AND HI SPATIAL DISTRIBUTION

Instead of describing individual ISM features qualitatively, an alternative way is to view them as they were produced with some random process (Lazarian 1995) and attempt to characterize them with a statistical descriptor. Many statistical descriptors have been used for such a purpose and some of their advantages and/or disadvantages can be found in Lazarian (1994) and Lazarian & Pogosyan (1997). We use here the 2-D spatial power spectra, for both HI and IR data, and the cross spectrum between the two. Although these statistical functions do not provide the complete description of the ISM, they give the hierarchy of scales on which structure is present in the ISM, allowing us, for example, to probe the topology of the ISM and the processes involved in its creation.

5.1 The spatial power spectrum of the IR intensities

We derive here the 2-D spatial power spectra of the IR intensity fluctuations at 60 and 100 μm (I_{60} and I_{100}). Both

Table 3. Comparison of the average dust-to-gas mass ratio in the SMC with previous work.

Reference	$N^*_{\rm HI}/E_{\rm B-V}$ (10^{22} atoms cm^{-2} mag^{-1})	$M^*_{\rm HI}/E_{\rm B-V}$ (10^{-2} g cm^{-2} mag^{-1})	$M_{\rm d}/M_{\rm HI}{}^a$ (10^{-5})	Method
Bouchet et al. (1985)	3.7	6.2	6.1	(2)
Martin et al. (1989)	4.6	7.7	7.5	(2)
Lequeux (1989)	5.0	8.4	8.1	(2)
Schwering (1988)	-	-	5.0	(1)
this paper	-	-	8.2	(1)

[a] Obtained using equation 11 for method (2).

images, I_{60} and I_{100}, were for this purpose first Fourier transformed. We call their Fourier transforms X_{60} and X_{100}, respectively. The average value of the square of the modulus of the transforms, $\langle X_{60}X^*_{60}\rangle$ and $\langle X_{100}X^*_{100}\rangle$, was then measured in 17 annuli of equal width in log $\sqrt{u^2+v^2}$ (u and v are the coordinates in the Fourier plane measured in units of λ and $*$ denotes a complex conjugate of a given function), in the same way as for the HI in Stanimirovic et al. (1999).

The resultant spectra are shown on Fig. 14. Both spectra can be well fitted by a power law, $P(k) \propto k^\gamma$ (where k represents spatial frequencies), over the linear size range $\sim$ 50 pc to $\sim$ 3 kpc, with $\gamma_{60} = -2.4 \pm 0.2$ for 60 μm band and $\gamma_{100} = -3.2 \pm 0.3$ for 100 μm band. However, the slopes steepen significantly around 50 pc, resulting in much steeper power spectra for smaller spatial scales. This might suggest that there is not enough IR small-scale structure to contribute to the power spectrum at these spatial scales. However, a significant power may be also missing on larger spatial scales ($>$ 50 pc) because of the quasi-blackbody cooling nature of dust grains, whereby the IR intensity fluctuations will be dominated by warm dust ($T \sim 50$ K), masking the real power of the cool dust ($T \sim 25$ K). From the discussion in Section 4.2, it appears that is not likely that so large amount of cool dust is missing to be able to influence sufficiently the spectrum over a wide range of larger spatial scales ($>$ 50 pc). It is likely though, that the cool dust may concentrate in small clumps, causing hence a significant underestimate of power on very small spatial scales, and therefore a change of the power-law slope.

The derived power-law index for 100 μm band is, nevertheless, similar to the indices found previously for the Galaxy. Gautier et al. (1992) have measured the spatial power spectrum for a few Galactic cirrus clouds at 100 μm, over the angular scale 2 arcmin to 8 deg, and found a good power law fit with an average slope of $\gamma = -3$. Recently, Schlegel, Finkbeiner & Davis (1998) have found a more shallow slope of $\gamma = -2.5$ from the full sky 100 μm maps for angular scales of 1.1 deg and over.

We now address the question of radial symmetry of the derived spatial power spectra. In the case when a significant preferred alignment of structure is present, caused by, for example, the tidal stretching or shear, the power spectra will significantly vary for different position angles (azimuth) in the Fourier plane. The azimuthal isotropy of the spatial power spectra has been tested for the Galaxy by Gautier et al. (1992), in case of dust, and by Green (1994), in case of HI, and no significant variation has been found. We perform here a similar test for the dust power spectra of the SMC. The same method for measuring a spatial power spectrum was applied on four different segments in the Fourier plane (with position angles 0°– 45°, 45°– 90°, 90°– 135°and 135°– 180°, respectively), performing data averaging in 17 annuli within each segment. The resultant spectra for 60 μm image are shown on Fig. 15. A possible systematic trend is visible for larger spatial scales. Values for third and fourth segments seem to be consistently lower than values for first and second segments. This shows that power spectra for third and fourth segments have more power on larger spatial scales, which corresponds to an alignment of structure in direction northeast–southwest, i.e. along the bar. However, all variations with azimuth seem to be small and within the estimated uncertainties, suggesting that derived spectra can be assumed to be radially symmetric.

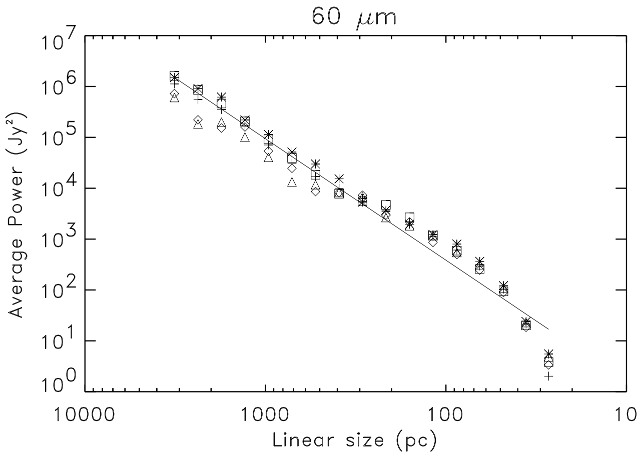

Figure 15. The 2-D spatial power spectra of the 60 μm intensity image over the linear size range $\sim$ 30 pc to $\sim$ 3 kpc. To test the azimuthal symmetry of the spatial power spectrum, radial averaging have been performed within four different segments in the Fourier plane: 0°– 45°(asterisk), 45°– 90°(square), 90°– 135°(diamond) and 135°– 180°(triangle). The radially averaged data points within the whole Fourier plane are shown with a plus sign (+) and overlaid with the least-square fit.

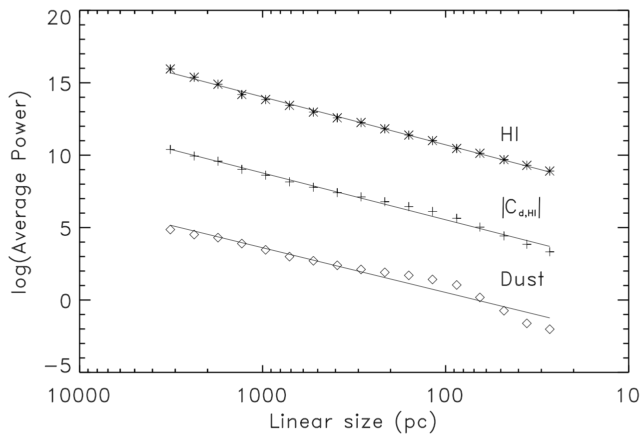

Figure 16. The 2-D spatial power spectra of dust and HI mass column densities, labeled as 'Dust' and 'HI' (in units of $M_\odot^2$), together with the spatial amplitude cross spectrum of dust and HI, labeled with $|C_{\rm d,HI}|$ (in units of $M_\odot$), which will be used in the next section.

5.2 Spatial power spectrum of HI and dust column densities

We turn now to the 2-D spatial power spectra of the dust and HI column densities. Both dust ($N_{\rm d}$) and HI ($N_{\rm HI}$) mass column density images were first Fourier transformed ($X_{\rm d}$ and $X_{\rm HI}$ are used to denote Fourier transforms of dust and HI, respectively). Assuming the azimuthal isotropy, tested in Section 5.1, the average value of the square of the modulus of the transforms, $\langle X_{\rm d} X_{\rm d}^* \rangle$ and $\langle X_{\rm HI} X_{\rm HI}^* \rangle$, was then measured in the usual way. Note that some masking was applied on $X_{\rm HI}$ to exclude four elliptical annuli where the ATCA data were not fully sampled (see Stanimirovic et al. 1999 for more information). Both dust ($P_{\rm d}$) and HI ($P_{\rm HI}$) spatial power spectra are shown on Fig. 16 labeled as 'Dust' and 'HI'.

Both $P_{\rm d}$ and $P_{\rm HI}$ are well fitted by a power law over a wide range of spatial scales (30 pc to 3.2 kpc). The power spectrum of the HI column density shows a remarkably tight power-law fit, $P_{\rm HI}(k) \propto k^{-3.31\pm0.01}$. The power spectrum of the dust column density can be fitted with $P_{\rm d}(k) \propto k^{-3.1\pm0.2}$, and is very similar to the spectrum of 100 μm intensity image. This spectrum also shows a slight change of slope on very small spatial scales (< 50 pc). Some deficiency of power on very large spatial scales may also be present, most likely due to the opacity effect and/or a lack of complete sampling on these spatial scales. Nevertheless, slopes for $P_{\rm d}$ and $P_{\rm HI}$ appear to be quite similar.

With thinner velocity slices (~ 5 km s^{-1}), the result $P_{\rm HI}(k) \propto k^{-3.05}$ was previously obtained using the same HI data (Stanimirovic et al. 1999). The spatial power spectrum of the HI mass column density (integrated along the whole velocity range, i.e. a 'thick' velocity slice) is presented here for the first time. There is a significant change in the power-law index from $\gamma = -3.04 \pm 0.02$ for 'thin' velocity slices to $\gamma = -3.31$ for a 'thick' velocity slice. The simple explanation is that integration along the velocity axis has washed out some small scale structure, leaving more power on the larger spatial scales. However, Lazarian & Pogosyan (1999) argue that the slope variation for different velocity slices contains important information about the origin of the spatial power spectrum. They show that 'thick' velocity slices represent HI density fluctuations, while 'thin' slices show the turbulent velocity fluctuations. The power spectra in Stanimirovic et al. (1999) therefore seem to have a significant velocity contribution.

The slope of $P_{\rm d}$ agrees well with the predictions by Padoan, Jones & Nordlund (1997), although very different approaches have been performed. In the investigation of the distribution of dust in dark molecular clouds by Lada et al. (1994), the simultaneous determination of colours for hundreds of stars was performed. A plot of the mean visual extinction (A_V) versus its dispersion (σ), $\sigma - A_V$, showed an interesting correlation which appears to have an important role in the study of structure of dark clouds. Padoan, Jones & Nordlund (1997) have shown that the $\sigma - A_V$ correlation originates in the strong fluctuations of the 3-D density distribution in dark clouds, produced by random supersonic motions. Their numerical simulations of the 3-D random density distribution shaped by supersonic flows show a power-law behavior of the spatial power spectra, $P(k) \propto k^{-2.6\pm0.5}$, which is consistent with observations of the cloud IC5146 by Lada et al. (1994). Projected in two dimensions, this results in the 2-D density fluctuation spectrum, with the slope between -3.0 and -3.1 (P. Padoan, private communication).

The power-law fit of both dust and HI column density power spectra shows that the hierarchical structure organization is present within dust and HI content of the ISM in the SMC, with no preferred spatial scales for dust and HI clouds. The power-law indices for dust and HI are similar, showing that similar processes are most likely involved in the shaping of both dust and HI content of the ISM. One interpretation of the $P(k)$ power-law, as discussed in Stanimirovic et al. (1999), is that the ISM in the SMC has a fractal nature, created by the supersonic turbulence. The mean slope of dust and HI power-law fits, $\langle \gamma \rangle = -3.2 \pm 0.1$, suggests the projected fractal dimension of $D_{\rm p} = 1.4 \pm 0.1$ (for relationship between the power spectrum and the projected fractal dimension see Stanimirovic et al. 1999), or the volume fractal dimension of $D = 2.4 \pm 0.1$, assuming a simple relationship $D = D_{\rm p} + 1$ suggested by Beech (1992). This is very similar to the measured volume fractal dimension for molecular clouds by Elmegreen & Falgarone (1996).

5.3 The spatial coherency spectrum

Finally, we investigate the statistical correlation between HI and dust column density using the cross spectrum, $C_{\rm d,HI} = \langle X_{\rm d} X_{\rm HI}^* \rangle$. $C_{\rm d,HI}$ is a complex function and its amplitude, $|C_{\rm d,HI}|$ (shown on Fig. 16), was used to derive the spatial coherency spectrum (Yuen & Fraser 1979) presented on Fig. 17:

$$K_{\rm d,HI}(k) = \frac{|C_{\rm d,HI}(k)|^2}{P_{\rm d}(k)\ P_{\rm HI}(k)}. \tag{12}$$

Some characteristics of the derived spatial and cross spectra in this paper are summarized in Table 4.

The spatial coherency spectrum is a measure of correlation between two functions on different spatial scales. Its values range between 0 and 1. In the case of two independent processes $K_{\rm d,HI}(k) = 0$ for all k, while $K_{\rm d,HI}(k) = 1$ (for all k) if one process is a linear function of the other one, or both processes are linear functions of some third random process.

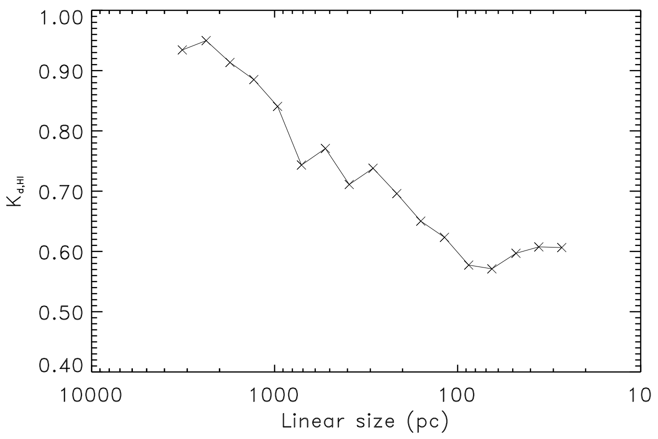

Figure 17. The spatial coherency spectrum of dust and HI mass column densities, $K_{\rm d,HI}(k)$.

Table 4. A summary of all $P(k) \propto k^{\gamma}$ slopes derived in this Paper.

	γ
60 μm intensity	-2.4 ± 0.2
100 μm intensity	-3.2 ± 0.3
HI 'thin' slices ($\sim$ 5 km s^{-1})	-3.04 ± 0.02
$N_{\rm d}$, dust column density	-3.1 ± 0.2
HI 'thick' slice, HI column density	-3.31 ± 0.01
$\left\|C_{\rm d,HI}\right\|$, cross spectrum	-3.23 ± 0.03

Fig. 17 shows that in general, dust and HI are spatially well correlated over a wide range of spatial scales. $K_{\rm d,HI}$ increases from $\sim$ 0.6 to $\sim$ 1, for spatial scales from $\sim$ 50 pc to the largest one used here to measure the power spectrum, $\sim$ 3.2 kpc. For very small spatial scales (30 – 50 pc), which mainly correspond to HII regions, no good correlation is expected because hydrogen here leaks, being either ionized or in molecular form. However, Fig. 17 shows on these scales a small bump in $K_{\rm d,HI}$. We note that this may be caused by an underestimate of cold dust on these spatial scales, as already discussed.

6 SUMMARY

We have presented here the high angular resolution far-infrared HIRAS images of the SMC, at 12, 25, 60 and 100 μm, for the first time. These images have angular resolutions of 1 arcmin at 12, 25 and 60 μm and 1.7 arcmin at 100 μm. The HIRAS data were used in conjunction with a combination of the ATCA and Parkes telescope HI spectral line surveys of the SMC to reach the following conclusions:

• The integrated HIRAS spectrum suggests that PAH molecules and VSGs do not play an important role in the SMC. The far-IR part of the spectrum can be reasonably well modeled with a composition of the quasi-blackbody curves for temperature range 15 – 30 K, showing that large dust grains in thermal equilibrium are predominantly responsible for IR emission at $\lambda \gtrsim 45$ μm. Assuming the standard dust model, dust temperature and dust column density distributions were derived. Dust temperatures range from 23 to 45 K which is warmer than for the Galaxy (17 – 30 K). While estimating the total mass of cool dust, it was found that the dust mass may be underestimated by $<$ 30% due to the presence of different temperature components along the line-of-sight, and altogether by $<$ 60% if the dust cooler than 20 K exists in the SMC. The total amount of cool dust in the SMC is thus $1.8^{+1.3}_{-0.2} \times 10^4$ M$_\odot$.

• The average dust-to-gas ratio in the SMC is, by mass, 8.2×10^{-5} (which is a factor of $\sim$ 30 below the Galactic value). The dust-to-gas mass ratio shows a significant spatial variation, decreasing considerably from the optical bar towards Eastern Wing. If interpreted as a deficiency of atomic gas, the mass of molecular hydrogen of $\sim 8 \times 10^8$ M$_\odot$ is required to account for this variation. This is about double the HI mass and about 10 – 30 times the mass accounted from CO studies. If interpreted as a deficiency of cold dust, a huge amount ($\sim 10^6$ M$_\odot$) must be present at temperatures of 9 K, or below, in order not be seen by COBE/DIRBE. Although a combination of both deficiencies most likely plays an important role, the existence of an intrinsic radial dependence of the dust-to-gas mass ratio, already found in several spiral galaxies, is very likely.

This radial dependence of the dust-to-gas mass ratio could be explained by the recent model for the dynamical and chemical dust evolution in the ISM (Dwek 1998). This model also predicts a tight correlation between the dust-to-gas ratio and metallicity. Using the correlation by Lisenfeld & Ferrara (1998) found from a sample of dwarf galaxies, we predict metallicity variations across the SMC. However, the current observational data for HII regions in the SMC appear to be not consistent with the proposed correlation.

• The 2-D spatial power spectra of the IR intensity at 60 and 100 μm, HI column density and dust column density, obey the relation, $P(k) \propto k^{\gamma}$. This suggests a hierarchical structure organization with no preferred sizes for dust and HI clouds. The power-law indices are reasonably similar for HI and dust column densities, with $\langle\gamma\rangle = -3.2$. One interpretation of the $P(k)$ power-law is that the dust and HI content of the ISM in the SMC have fractal nature with the volume fractal dimension of $D = 2.4$. This is similar to values obtained by other authors for molecular clouds in the Galaxy and may imply similar mechanisms for structure formation.

• The spatial coherency spectrum shows that dust and HI are well correlated for spatial scales larger than 50 pc, with the correlation coefficient ranging between 0.6 and 1.

The high resolution IRAS data of the SMC at 12, 25, 60 and 100 μm, as well as the HI and dust column density images, are available electronically from the ATNF SMC web page (see http://www.atnf.csiro.au/research/smc_h1/).

ACKNOWLEDGMENTS

We want to thank Jeroen van Hoof and Willem Vermin of the SARA computing center in Amsterdam for their support and advice on the use of their computing equipment, as well as Walter Hoffman and Dick van Albada of the Computational Science institute. We are grateful to Jim Caswell, Raymond Haynes and an anonymous referee for their beneficial comments on this paper. We thank K. Brooks, B. Köribalski, J. Dickey, R. Ekers, A. Lazarian and P. Padoan for stimulating and fruitful discussions. We acknowledge use of the KARMA visualization software for some figures (Gooch 1995). SS also wishes to acknowledge the Kapteyn Astronomical Institute and Laboratorium voor Ruimteonderzoek, SRON, for their kind hospitality during one part of data analyses, and the University of Western Sydney Nepean for travel support. TjRB acknowledges financial support provided by the Netherlands Organization for Scientific Research (NWO) through its Massive Parallel Computing (MPR) program.

REFERENCES

Alton P.B. et al., 1998, A&A, 335, 807
Assendorp, R., Bontekoe, T.R., de Jonge, A.R.W., Kester, D.J.M., Roelfsema, P.R., Wesselius, P.R., 1995, A&AS, 110, 395.
Aumann, H.H., Fowler, J.W., Melnyk, M., 1990, AJ, 99, 1674
Beech M., 1992, Ap&SS, 192, 103B
Beichman C.A., Neugebauer G., Habing H.J., Clegg P.E., Chester T.J., 1985, Infrared Astronomical Satellite Catalogs and Atlases. Explanatory Supplement. Jet Propulsion Lab., California Inst. of Tech., Pasadena, p. VII-1, VI-27
Bontekoe Tj.R., Koper E., Kester D.J.M., 1994, A&A, 284, 1037
Bouchet P., Lequeux J., Maurice E., Prevot L., Prevot-Burnichon M.L., 1985, A&A, 149, 330
Boulanger F., Abergel A., Bernard J.-P., Burton W.B., Desert F.-X., Hartmann D., Lagache G., Puget J.-L., 1996, A&A, 312, 256
Cao Y., Prince T.A., Terebey S., Beichman C., 1999, AJ, submitted
Copetti M.V.F., 1990, A&A, 229, 533
Cox P., Mezger P.G., 1989, A&AR, 1, 49C
Davies, R.D., Elliot, K.H., Meaburn, J., 1976, Mem. R. astr. Soc. 81, 89D.
de Vaucouleurs G., de Vaucouleurs A., Corwin H. G., Buta R. J., Paturel G., Fouque P., 1991, Copy-editing: Third reference catalogue of bright galaxies. Springer-Verlag, New York
Draine B.T., 1990, in Thronson Jr. H.A. & Shull J.M., eds, The Interstellar Medium in Galaxies. Kluwer, Dordrecht, p. 483
Draine B.T., Anderson N., 1985, ApJ, 292, 494
Dufour R.J., Harlow W.V., 1977, ApJ, 216, 706
Dwek E., 1998, ApJ, 501, 643
Dwek E. et al., 1997, ApJ, 475, 565
Dyson J.E., Williams D.A., 1997, Physics of the interstellar medium. Institute of Physics Publishing, Bristol, England, p. 25
Elmegreen B.G., Falgarone E., 1996, ApJ, 471, 816
Evans A., 1994, The Dusty Universe. John Wiley & Sons, Praxis Publishing, Chichester, p. 54
Gautier T.N., Boulanger F., Perault M., Puget J.L., 1992, AJ, 103(4), 1313
Gooch R.E., 1995, in Shaw R.A., Payne H.E., Hayes J.J.E., eds, ASP Conf. Ser. Vol. 77, Astronomical Data Analysis and Software Systems V. Astron. Soc. Pac., San Francisco, p. 144
Gordon K.D., Clayton G., 1998, ApJ, 500, 816
Gordon, M.A., 1988, in Kellermann K., Verschur G.L., eds, Galactic ans Extragalactic Radio Astronomy. Springer-Verlag, New York, p. 37
Green D.A., 1994, Ap&SS, 216, 201
Gull S.F., Skilling J., 1991, MEMSYS5 Users Manual. Maximum Entropy Data Consultants Ltd.
Hauser M.G., Kelsall T., Leisawitz D., Weiland J., 1998, COBE Diffuse Infrared Background Experiment (DIRBE) Explanatory Supplement. COBE Ref. Pub. No. 98-A (Greenbelt, MD: NASA/GSFC), available in electronic form from NSSDC, p. 113
IRAS point source catalog, Version 2, 1988, Joint IRAS Science Working Group, U.S. Goverment Printing Office, Washington D.C.
Israel F.P., 1997, A&A, 328, 471
Israel F.P., Koornneef J., 1988, A&A, 190, 21
Israel F.P., Maloney P.R., Geis N., Herrmann F., Madden S.C., Poglitsch A., Stacey G.J., 1996, ApJ, 465, 738
Issa M.R., MacLaren I., Wolfendale A.W., 1990, A&A, 236, 237
Kester D.J.M., Bontekoe Tj.R., 1994, in Terebey S., Mazzarella J., eds, Science with High Spatial Resolution Far-Infrared Data. JPL Publication 94-5, p. 23
Knapp G.R., 1990, in Thronson H.A., Shull J.M., eds, The Interstellar Medium in Galaxies. Kluwer Academic Publishers, p. 3
Koornneef J., 1982, A&A, 107, 247
Koornneef J., 1984, in van der Bergh S., de Boer K.S., eds, Proc IAU Symp. 108, Structure and Evolution of the Magellanic Clouds. D. Reidel Publishing Co., Dordrecht, p. 333
Koornneef J., Israel F.P., 1985, ApJ, 291, 156
Kulkarni S.R., Heiles C., 1988, in Kellermann K., Verschur G.L., eds, Galactic ans Extragalactic Radio Astronomy. Springer-Verlag, New York, p. 107
Kurt C.M., Dufour R.J., Garnett D.R., Skillman E.D., Mathis J.S., Peimbert M., Torres-Peimbert S., Walter D.K., 1995, RMxAA, 3, 223K
Kurt C.M., Dufour R.J., 1998, RMxAA, 7, 202K
Lada C.J., Lada E.A., Clemens D.P., Bally J., 1994, ApJ, 429, 694
Lazarian A., 1994, Ap&SS, 216, 207L
Lazarian A., 1995, A&A, 293, 507L
Lazarian A., Pogosyan D., 1997, ApJ, 491, 200L
Lazarian A., Pogosyan D., 1999, submitted to ApJ
Lequeux, J., 1989, in de Boer K.S., Spite F., Stasinska G., eds, Recent Developments of MC Research. Meudon, France, p. 119
Li A., Greenberg J.M., 1997, A&A, 323, 566
Lisenfeld U., Ferrara A., 1998, ApJ, 496, 145
Low F.J. et al., 1984, ApJ, 278L, 19L
Martin N., Maurice E., Lequeux J., 1989, A&A, 215, 219
Mathis J.S., Rumpl W., Nordsieck K.H., 1977, ApJ, 217, 425M
McGee R.X., Newton L.M., 1981, PASA, 4, 189M
Murai T., Fujimoto M., 1980, PASJ, 32, 581
Padoan P., Jones B.J., Nordlund A.P., 1997, ApJ, 474, 730
Pagel B.E.J., Edmunds M.G., Fosbury R.A.E., 1978, MNRAS, 184, 569
Putman M.E. et al., 1998, Nature, 394, 752
Reach W.T. et al., 1995, ApJ, 451, 188
Reach W.T., Wall W.F. & Odegard N., 1998, ApJ, 507, 507
Rice W., 1993, AJ, 105, 67R
Rodrigues C.V., Magalhaes A.M., S.J. Coyne G.V., Piirola V., 1997, ApJ, 485, 618
Rubio M., Lequeux J., Boulanger F., 1993, A&A, 271, 9
Sauvage M., Vigroux L., 1991, in Haynes R.F., Milne D.K., eds, Proc IAU Symp. 148, The Magellanic Clouds. Kluwer, Dordrecht, p. 407
Schlegel D.J., Finkbeiner D.P., Davis M., 1998, ApJ, 500, 525
Schwering P., 1988, PhD thesis, Sterrewacht Leiden
Schwering P.B.W., Israel F.P., 1989, A&AS, 79, 79
Sivia D.S., 1996, Data analysis, a Bayesian tutorial. Clarendon Press, Oxford
Sodroski T.J. et al., 1994, ApJ, 428, 638

Sodroski T.J., Odegard N., Arendt R.G., Dwek E., Weiland J.L., Hauser M.G., Kelsall T., 1997, ApJ, 480, 173
Stanimirovic S., Staveley-Smith L., Dickey J.M., Sault R.J., Snowden S.L., 1999, MNRAS, 302, 417
Staveley-Smith L., Sault R.J., Hatzidimitriou D., Kesteven M.J., McConnell D., 1997, MNRAS, 289, 225
Staveley-Smith L., Kim S., Putman M., Stanimirovic S., 1998, Rev. Mod. Astron., 11, 117
van der Hulst J.M., Kennicutt R.C., Crane P.C., Rots A.H., 1988, A&A, 195, 38
Viallefond F., Goss W.M., Allen R.J., 1982, A&A, 115, 373
Viallefond F., Goss W.M., 1986, A&A, 154, 357
Walterbos, R.A.M., Schwering P.B.W., 1987, A&A, 180, 27
Westerlund B.E., 1991, in Haynes R.F., Milne D.K., eds, Proc IAU Symp. 148, The Magellanic Clouds. Kluwer, Dordrecht, p. 15
Wheelock S.L. et al., 1994, IRAS Sky Survey Atlas: Explanatory Supplement. Jet Propulsion Lab., California Inst. of Tech., Pasadena, CA, p. IV-16
Young E.T., Neugebauer G., Kopan E.L., Benson R.D., Conrow T.P., Rice W.L., Gregorich D.T., 1985, A user's guide to IRAS pointed observation products. IPAC Report
Yuen C.K., Fraser D., 1979, Digital Spectral Analysis. CSIRO/Pitman, Adelaide, Australia, p. 59
Zubko V.G., 1999, ApJ, 513, L29